Supplementary Information for "Rapid planetesimal formation in turbulent circumstellar discs"

Abstract

This document contains refereed supplementary information for the paper "Rapid planetesimal formation in turbulent circumstellar discs". It contains 15 sections (§1.1 – §1.15) that address a number of subjects related to the main paper. Some of the subjects are highlighted here in the abstract. We describe in detail the Poisson solver used to find the self-potential of the solid particles, including a linear and a non-linear test problem (§1.3). Dissipative collisions remove energy from the motion of the particles by collisional cooling (§1.4), an effect that allows gravitational collapse to occur in somewhat less massive discs (§1.7). A resolution study of the gravitational collapse of the boulders is presented in §1.6. We find that gravitational collapse can occur in progressively less massive discs as the grid resolution is increased, likely due to the decreased smoothing of the particle-mesh self-gravity solver with increasing resolution. In §1.10 we show that it is in good agreement with the Goldreich & Ward (1973) stability analysis to form several-hundred-km-sized bodies, when the analysis is applied to 5 AU and to regions of increased boulder column density. §11 is devoted to the measurement of random speeds and collision speeds between boulders. We find good agreement between our measurements and analytical theory for the random speeds, but the measured collision speeds are 3 times lower than expected from analytical theory. Higher resolution studies, and an improved analytical theory of collision speeds that takes into account epicyclic motion, will be needed to determine whether collision speeds have converged. In §1.12 we present models with no magnetic fields. The boulder layer still exhibits strong clumping, due to the streaming instability, if the global solids-to-gas ratio is increased by a factor 3. Gravitational collapse occurs as readily as in magnetised discs.

Authors:

Anders Johansen[1], Jeffrey S. Oishi[2,3], Mordecai-Mark Mac Low[2,1], Hubert Klahr[1], Thomas Henning[1] & Andrew Youdin[4]

Affiliations:

1. Max-Planck-Institut für Astronomie, Königstuhl 17, D-69117 Heidelberg, Germany
2. Department of Astrophysics, American Museum of Natural History, 79th Street at Central Park West, New York, NY 10024-5192, USA
3. also Department of Astronomy, University of Virginia, Charlottesville, VA, USA
4. Canadian Institute for Theoretical Astrophysics, University of Toronto, 60 St. George Street, Toronto, Ontario M5S 3H8, Canada

1 Supplementary Discussion

1.1 Pencil Code

The Pencil Code[31] is a finite difference code that uses symmetric derivatives of sixth order in space and a third order Runge-Kutta time-stepping scheme. The difference equations as implemented are formally dissipation free, having phase errors but no amplitude error. Only a small amount of numerical dissipation is introduced from time-stepping the advection term. Therefore, one must explicitly add dissipation to the dynamical equations to suppress numerically unstable modes near the grid scale and to dissipate the turbulent energy that is (in our case) released from the Keplerian shear by the Reynolds and Maxwell stresses. For this purpose, we use sixth order hyperdiffusivity operators, where the usual ∇^2 diffusivity operator is replaced with a ∇^6 operator[32,33]. Hyperdiffusivity dissipates energy at high wave numbers – at the smallest scales in the simulation – but preserves energy at low wave numbers. Hyperviscosity and magnetic hyperresistivity have been used extensively to study the properties of forced magnetohydrodynamic turbulence (see Brandenburg & Sarson[34] and references therein). They are designed to affect large scales as little as possible by dissipation, thus widening the inertial range beyond what can be achieved with a regular viscosity operator while still maintaining numerical stability. We have tested that particle overdensities occur for both the stringent hyperviscosity scheme used by Haugen & Brandenburg[32] and for the simplified scheme described in Johansen & Klahr[33].

Possible side effects of using hyperviscosity and hyperresistivity include an artificial increase in the bottleneck effect[35], a physical effect in turbulence where energy piles up around the dissipative scale, and a higher saturation level for dynamo-generated magnetic fields in helical flows compared to what is seen when using a regular viscosity operator[34]. The bottleneck effect is unlikely to be relevant to the dynamics of boulders in turbulence, since marginally coupled particles are mostly affected by turbulent structures at the largest scales of our simulation where the bottleneck effect is unimportant. The saturation level of turbulence driven by the magnetorotational instability (MRI) is indeed affected by the numerical scheme and by the dissipation scheme, but the Pencil Code agrees well with other grid codes regarding the statistical properties of MRI turbulence[14,36].

1.2 Drag force

1.2.1 Drag force algorithm

The computation of drag forces between Lagrangian particles and an Eulerian grid requires some care to avoid spurious accelerations and to ensure momentum conservation. Small errors in the gas velocity can be dangerously amplified by the subtraction of highly correlated particle velocities. Tests of our drag force algorithm are described in detail elsewhere[37]. It involves three steps:

1. Interpolate gas velocities at particle positions.

2. Calculate the drag force on the particles from the gas in nearby cells.

3. Assign the back-reaction force to the gas from particles in nearby cells.

For the first step, interpolation, we begin with gas velocities, $\boldsymbol{u}^{(\boldsymbol{j})}$, defined on a uniform grid where the index $\boldsymbol{j}$ labels the cells centred on positions $\boldsymbol{x}^{(\boldsymbol{j})}$. We interpolate to the particle positions, $\boldsymbol{x}^{(i)}$, using a weight function, $W_{\rm I}$, as

$$\overline{\boldsymbol{u}(\boldsymbol{x}^{(i)})} = \sum_{\boldsymbol{j}} W_{\rm I}(\boldsymbol{x}^{(i)} - \boldsymbol{x}^{(\boldsymbol{j})})\boldsymbol{u}^{(\boldsymbol{j})} \,. \tag{1}$$

The weight function is normalised as $\sum_{\boldsymbol{j}} W_{\rm I}(\boldsymbol{x}^{(i)} - \boldsymbol{x}^{(\boldsymbol{j})}) = 1$, for any $\boldsymbol{x}^{(i)}$, and has non-zero contributions only from the cells in the immediate vicinity of $\boldsymbol{x}^{(\boldsymbol{j})}$.

The second step, calculating the drag acceleration on particle i,

$$\boldsymbol{f}_{\rm p}^{(i)} = -\frac{1}{\tau_{\rm f}}\left[\boldsymbol{v}^{(i)} - \overline{\boldsymbol{u}(\boldsymbol{x}^{(i)})}\right] \,, \tag{2}$$

is trivial once the relevant quantities are defined. We assume that the drag force is proportional to the velocity difference between gas and particles, i.e. that the friction time $\tau_{\rm f}$ is independent of the velocity difference.

Finally, we calculate the back-reaction drag force, $\boldsymbol{f}_{\rm g}^{(\boldsymbol{j})}$, on the gas in cell $\boldsymbol{j}$. Assigning the particle velocities to a grid risks violating momentum conservation. Instead we use Newton's third law to directly assign the force on the particles back to the gas,

$$\boldsymbol{f}_{\rm g}^{(\boldsymbol{j})} = -\frac{m_{\rm p}}{\rho_{\rm g}^{(\boldsymbol{j})} V_{\rm cell}} \sum_i W_{\rm A}(\boldsymbol{x}^{(i)} - \boldsymbol{x}^{(\boldsymbol{j})})\boldsymbol{f}_{\rm p}^{(i)} \,, \tag{3}$$

where $m_{\rm p}$ is the mass of a superparticle, $\rho_{\rm g}^{(\boldsymbol{j})}$ is the gas density in cell $\boldsymbol{j}$, and $V_{\rm cell}$ is the volume of a grid cell. The assignment function $W_{\rm A}$ obeys the same conditions as $W_{\rm I}$, so that only particles in a given cell or in that cell's nearby neighbours contribute to the sum. We opt for the second order Triangular Shaped Cloud (TSC) assignment scheme[19], which uses an identical function for assignment and for interpolation, $W_{\rm A} = W_{\rm I}$. The TSC spreads the influence of particles and grid points to three grid points in each direction, for a total of 27 points in three-dimensional (3-D) simulations.

The interpolation errors associated with the TSC assignment is found by considering a periodic function (of arbitrary phase) sampled at the grid points[19,37]. The result is that the assigned amplitude of a single Fourier component at scale k relative to the actual amplitude is to second order $1 - (\Delta k)^2/8$, where Δ is the linear size of a grid cell. Thus already at 5 grid cells there is significant smoothing. This smoothing is found to have an influence on the gravitational collapse, especially at crude resolution, see §1.6.

The time-step constraint set by the drag force is $\delta t_{\rm drag} = \tau_{\rm f}/(1+\epsilon)$, where ϵ is the local solids-to-gas ratio[11]. As the solids-to-gas ratio increases, the allowed time-step decreases. We have made sure that the friction time-step never dominates over the Courant time-step of the code by artificially increasing the friction time in regions of high solids-to-gas ratio ($\epsilon > 100$). We have experimented with the threshold and found no improved collapse for a higher threshold, presumably because inelastic collisions dominates the kinetic energy dissipation at these densities anyway.

1.2.2 Particle sizes and drag regimes

In our work, as in most theoretical work, we characterise particles in terms of their dimensionless friction time $\Omega_{\rm K}\tau_{\rm f}$ (where $\Omega_{\rm K}$ is the Keplerian orbital frequency). The translation to a particle size depends on the assumed disc model. The smallest particles are subject to Epstein drag, valid when the particle radius is smaller than the mean free path of the gas (see below), with

$$\Omega_{\rm K}\tau_{\rm f}^{\rm (Ep)} = \frac{\Omega_{\rm K}\rho_\bullet a}{\rho_{\rm g} c_{\rm s}} = \sqrt{2\pi}\frac{\rho_\bullet a}{\Sigma_{\rm g}}\,, \tag{4}$$

where the second step applies in the disc midplane. Here $\rho_\bullet$ is the material density of the solids, a is the radius of a solid body, $\rho_{\rm g}$ is the gas density, $c_{\rm s}$ is the sound speed, while $\Sigma_{\rm g}$ is the column density of gas. Epstein drag depends on gas density, but in practice the gas density fluctuations are negligible (order 1%) in our subsonic flows, so we ignore them. Solving for particle size gives

$$a = \frac{\Omega_{\rm K}\tau_{\rm f}^{\rm (Ep)}\Sigma_{\rm g}}{\sqrt{2\pi}\rho_\bullet} \approx 30\,{\rm cm}\,\Omega_{\rm K}\tau_{\rm f}^{\rm (Ep)}\left(\frac{\Sigma_{\rm g,5}}{150\,{\rm g\,cm^{-2}}}\right)\left(\frac{\rho_\bullet}{2\,{\rm g\,cm^{-3}}}\right)^{-1}\left(\frac{r}{5\ {\rm AU}}\right)^{-1.5}\,, \tag{5}$$

where the normalisation of the gas surface density at 5 AU, $\Sigma_{\rm g,5}$, and the power law slope follows the minimum mass solar nebula model[38]. Applying a simulation with given $\tau_{\rm f}$ values to different disc radii changes the relevant particle sizes. Considering, as in the main text, $r = 5\,{\rm AU}$ and $\Sigma_{\rm g} = 300\,{\rm g\,cm^{-2}}$ yields particle sizes of $a = 60, 45, 30, 15$ cm, for $\Omega_{\rm K}\tau_{\rm f} = 1.0, 0.75, 0.5, 0.25$, respectively. When the model is applied to the outer solar nebula at $r = 40\,{\rm AU}$ instead, the corresponding particle sizes are as low as a few centimetres (per $\Omega_{\rm K}\tau_{\rm f}$).

The Epstein regime of free molecular (or Knudsen) flow ceases to apply once the particle radius exceeds (9/4 of) the gas mean free path,

$$\lambda = \frac{\mu}{\rho_{\rm g}\sigma_{\rm mol}} = \frac{\sqrt{2\pi}\mu H}{\Sigma_{\rm g}\sigma_{\rm mol}} \tag{6}$$

$$\approx 1\,{\rm m}\left(\frac{\Sigma_{\rm g,5}}{150\,{\rm g\,cm^{-3}}}\right)^{-1}\frac{H/r}{0.04}\left(\frac{r}{5{\rm AU}}\right)^{2.5}\,, \tag{7}$$

where $\mu = 3.9\times10^{-24}$ g is the mean molecular weight and $\sigma_{\rm mol} = 2\times10^{-15}{\rm cm}^2$ is the molecular cross section of molecular hydrogen[39,40]. The radial dependence does not include flaring of the aspect ratio, H/r. Epstein drag applies as long as

$$\Omega_{\rm K}\tau_{\rm f}^{\rm (Ep)} < \frac{9\pi}{2}\frac{\rho_\bullet\mu H}{\Sigma_{\rm g}^2\sigma_{\rm mol}} \approx 7\left(\frac{\rho_\bullet}{2\,{\rm g\,cm^{-3}}}\right)\left(\frac{\Sigma_{\rm g,5}}{150\,{\rm g\,cm^{-2}}}\right)^{-2}\left(\frac{H/r}{0.04}\right)\left(\frac{r}{5\,{\rm AU}}\right)^{4}\,. \tag{8}$$

Thus Epstein drag is the relevant regime for the application of our model to 5 AU.

Extrapolation of our model to higher column densities (or regions closer to the star) requires consideration of Stokes drag, for which

$$\Omega_{\rm K}\tau_{\rm f}^{\rm (St)} = \Omega_{\rm K}\tau_{\rm f}^{\rm (Ep)}\frac{4a}{9\lambda} = \frac{4\rho_\bullet a^2\sigma_{\rm mol}}{9\mu H}\,. \tag{9}$$

Since Stokes drag is also linear in the relative velocity between gas and solids, our model applies with a different scaling of particle size,

$$a = \left[\frac{9\Omega_{\rm K}\tau_{\rm f}^{\rm (St)}\mu H}{4\rho_\bullet\sigma_{\rm mol}}\right]^{1/2} \approx 80\,{\rm cm}\left[\Omega_{\rm K}\tau_{\rm f}^{\rm (St)}\left(\frac{\rho_\bullet}{2\,{\rm g\,cm^{-3}}}\right)^{-1}\left(\frac{H/r}{0.04}\right)\left(\frac{r}{5{\rm AU}}\right)\right]^{1/2}. \tag{10}$$

Actually since Stokes drag is independent of gas density (including fluctuations), our model is more exact in this regime, but modelling particles in the Stokes regime would require a different treatment of collisional cooling (see §1.4).

1.2.3 Energy dissipation by drag force

The dissipation of kinetic energy caused by drag force can be calculated as

$$\dot{e}_{\rm kin} = \boldsymbol{u}\cdot\left(\rho_{\rm g}\frac{\partial\boldsymbol{u}}{\partial t}\right)_{\rm drag} + \boldsymbol{w}\cdot\left(\rho_{\rm p}\frac{\partial\boldsymbol{w}}{\partial t}\right)_{\rm drag}, \tag{11}$$

where $\boldsymbol{u}$ and $\boldsymbol{w}$ are the respective gas and particle velocity fields. We refer to references [41] and [42] for considerations of the effect of drag force damping on the dynamics of particles. Inserting the fluid expressions for the drag force acceleration,

$$\frac{\partial\boldsymbol{u}}{\partial t} = -\frac{\rho_{\rm p}/\rho_{\rm g}}{\tau_{\rm f}}(\boldsymbol{u}-\boldsymbol{w}), \tag{12}$$

$$\frac{\partial\boldsymbol{w}}{\partial t} = -\frac{1}{\tau_{\rm f}}(\boldsymbol{w}-\boldsymbol{u}), \tag{13}$$

yields

$$\dot{e}_{\rm kin} = -\frac{\rho_{\rm p}}{\tau_{\rm f}}|\boldsymbol{w}-\boldsymbol{u}|^2. \tag{14}$$

Dissipation of kinetic energy by drag forces comes automatically when applying the momentum-conserving drag force. We usually assume that the dissipated energy can immediately radiate away efficiently, keeping the temperature of the gas constant. We show, however, in §1.13 that even if all the released energy remains locally as heat, the resulting temperature increase of the gas is insignificant and has no influence on the initial stages of the gravitational collapse.

As long as there is a velocity difference between the solid particles and the surrounding gas, then drag force cooling is efficient according to equation (14). But the relative speed of gas and particles in drag force equilibrium decreases with increasing solids-to-gas ratio [39], as the solid particles entrain the gas. In that case inelastic collisions take over as the dominant cooling mechanism (see §1.4).

1.3 Self-gravity solver

We compute the gravitational potential Φ of the particles by determining a particle density on the mesh and solving the Poisson equation for this assigned density field. The gravitational acceleration is then interpolated back to the positions of the particles. The particles are

assigned to the mesh using the TSC scheme[19], spreading each particle over the 27 nearest grid points (in 3-D), and the gravitational acceleration is added back to the particles using a second order spline interpolation to avoid any risk of self-acceleration of the particles.

The Poisson equation,

$$\nabla^2 \Phi = 4\pi G \rho_{\rm p} \,, \tag{15}$$

where G is the gravitational constant and $\rho_{\rm p}$ is the assigned particle density field, is solved using a Fourier method. The solution for a single Fourier density mode of wave number $\boldsymbol{k} = (k_x, k_y, k_z)$ and complex Fourier amplitude $\rho_{\boldsymbol{k}}$ is

$$\Phi_{\boldsymbol{k}} = -\frac{4\pi G \rho_{\boldsymbol{k}}}{k^2} \tag{16}$$

for $k = |\boldsymbol{k}| > 0$. The full potential is then $\Phi(\boldsymbol{x}) = \sum_{\boldsymbol{k}} \Phi_{\boldsymbol{k}} \exp[{\rm i}\boldsymbol{k} \cdot \boldsymbol{x}]$.

The radial x-direction in the shearing sheet is not strictly periodic, but is rather shear periodic with the connected points at the inner and outer boundary separated by the distance $\Delta y(t) = \mathrm{mod}[(3/2)\Omega_{\rm K} L_x t, L_y]$ in the y-direction. We follow the algorithm of Gammie[20] to include shear-periodic boundaries in the Fourier method, with the difference that we perform the necessary interpolation in Fourier space rather than in real space, as suggested by C. McNally at `http://imp.mcmaster.ca/~colinm/ism/rotfft.html`. First we apply a discrete Fast Fourier Transform (FFT) in the periodic y-direction. We then shift the entire y-direction by the amount $\delta y(x) = \Delta y(t) x / L_x$ to make the x-direction periodic, before proceeding with discrete FFTs along x and then z. Performing the $\delta y(x)$ shift in Fourier space (essentially using a Fourier interpolation method) has the advantage over polynomial interpolation that it is continuous and smooth in all its derivatives. After solving the Poisson equation in Fourier space, using the algebraic solution from equation (16), we transform the potential back to real space in the opposite order, shifting the y-direction back to the sheared frame on the way.

The gravitational constant G in equation (15) must be defined in code units. We adopt the unit system $\Omega_{\rm K} = c_{\rm s} = H = \rho_{\rm g,mid} = 1$, where the parameters are respectively the Keplerian frequency, isothermal sound speed, pressure scale height, and midplane gas density of the disc. The non-dimensional form of the Poisson equation is

$$(H\nabla)^2 \Phi / c_{\rm s}^2 = \tilde{G} \frac{\rho_{\rm p}}{\rho_{\rm g,mid}} \,, \tag{17}$$

where

$$\tilde{G} \equiv 4\pi G \rho_{\rm g,mid} \Omega_{\rm K}^{-2} \tag{18}$$

is a self-gravity parameter which relates to the Toomre parameter[43] Q of self-gravitating gas discs as

$$Q \approx 1.6 \tilde{G}^{-1} \,. \tag{19}$$

In case of vertical hydrostatic equilibrium the connection between the midplane density $\rho_{\rm g,mid}$ and the column density $\Sigma_{\rm g}$ is $\rho_{\rm g,mid} = \Sigma_{\rm g} / (\sqrt{2\pi} H)$. Introducing further the dimensionless scale-height-to-radius parameter H/r yields the power law connection

$$\Sigma_{\rm g} = 300\,{\rm g\,cm^{-2}} \left(\frac{\tilde{G}}{0.1} \right) \left(\frac{H/r}{0.04} \right) \left(\frac{M_\star}{M_\odot} \right) \left(\frac{r}{5\,{\rm AU}} \right)^{-2} \,. \tag{20}$$

Here we have made use of the identity $\Omega_{\rm K}^2 = GM_\star/r^3$, where $M_\star$ is the mass of the central gravity source and r is the orbital radius to a considered point in the disc.

1.3.1 Testing the Poisson solver

We validate here the FFT Poisson solver for a complex test case of a self-gravitating, shearing particle wave with gas drag. This is not a standard test problem, but we found it very useful for validating the particle-mesh self-gravity scheme of the Pencil Code. The particle density, velocity and self-potential are written as $\rho_{\rm p} = \rho_0 + \rho'_{\rm p}$, $\boldsymbol{w} = \boldsymbol{w}_0 + \boldsymbol{w}'$, $\Phi = \Phi_0 + \Phi'$. Here $\boldsymbol{w}_0 = u_y^{(0)}\hat{\boldsymbol{y}} \equiv -(3/2)\Omega_{\rm K} x\hat{\boldsymbol{y}}$ is the Keplerian shear flow. The linearised continuity equation, equation of motion and Poisson equation are

$$\partial_t \rho'_{\rm p} + u_y^{(0)}\partial_y \rho'_{\rm p} = -\rho_0(\partial_x w'_x + \partial_y w'_y)\,, \tag{21}$$

$$\partial_t w'_x + u_y^{(0)}\partial_y w'_x = 2\Omega_{\rm K} w'_y - \partial_x \Phi' - \frac{1}{\tau_{\rm f}} w'_x, \tag{22}$$

$$\partial_t w'_y + u_y^{(0)}\partial_y w'_y = -\frac{1}{2}\Omega_{\rm K} w'_x - \partial_y \Phi' - \frac{1}{\tau_{\rm f}} w'_y\,, \tag{23}$$

$$\nabla^2 \Phi' = 4\pi G \rho'_{\rm p}. \tag{24}$$

Here we have assumed particle motion to take place in the radial-azimuthal plane and zero gas velocity, $u_x = u_y = 0$, in the friction terms. Because of the Keplerian shear flow, the coefficients of the linearised equations are not independent of t, and thus an eigenmode analysis is not possible. Instead, we assume a separable solution $q(t,x,y) = \hat{q}(t)\exp[{\rm i}(k_x(t)x + k_y y)]$ for each dynamical variable. The time derivative of $q(t,x,y)$ is

$$\dot{q}(t,x,y) = [\partial_t \hat{q}(t) + \hat{q}(t) i x \partial_t k_x(t)]\exp[{\rm i}(k_x(t)x + k_y y)]\,. \tag{25}$$

By setting $x\partial_t k_x(t) = -u_y^{(0)} k_y$, we cancel the $u_y^{(0)}\partial_y q$ terms in equations (21)–(23), leaving a system of equations for $(\hat{\rho}_{\rm p}, \hat{w}_x, \hat{w}_y)$,

$$\frac{{\rm d}\hat{\rho}_{\rm p}}{{\rm d}t} = -\rho_0 {\rm i}(k_x \hat{w}_x + k_y \hat{w}_y)\,, \tag{26}$$

$$\frac{{\rm d}\hat{w}_x}{{\rm d}t} = 2\Omega_{\rm K}\hat{w}_y + \frac{4\pi {\rm i} G k_x \hat{\rho}_{\rm p}}{k_x^2 + k_y^2} - \frac{1}{\tau_{\rm f}}\hat{w}_x\,, \tag{27}$$

$$\frac{{\rm d}\hat{w}_y}{{\rm d}t} = -\frac{1}{2}\Omega_{\rm K}\hat{w}_x + \frac{4\pi {\rm i} G k_y \hat{\rho}_{\rm p}}{k_x^2 + k_y^2} - \frac{1}{\tau_{\rm f}}\hat{w}_y\,, \tag{28}$$

together with $k_x(t) = k_x(t_0) + (3/2)\Omega_{\rm K} t k_y$.

We solve this system of ordinary differential equations numerically using a third order Runge-Kutta method to follow the temporal evolution of a non-axisymmetric wave with the initial condition $k_x = -1, k_y = 1, \hat{w}_x = \hat{w}_y = 0, \hat{\rho}_{\rm p} = 10^{-4}$, and $G = \Omega_{\rm K} = \rho_0 = \tau_{\rm f} = 1$. This semi-analytic solution is then compared to the evolution obtained with the full solver of the Pencil Code (64^2 grid points and 4 particles per cell). Because we use particles to represent the solids and a grid-based FFT solver to calculate the gravitational potential, the comparison provides an excellent of test of all physics and numerical schemes relevant to our investigation: numerical particles, grid-based FFT self-gravity, shear and shear-periodic boundary conditions.

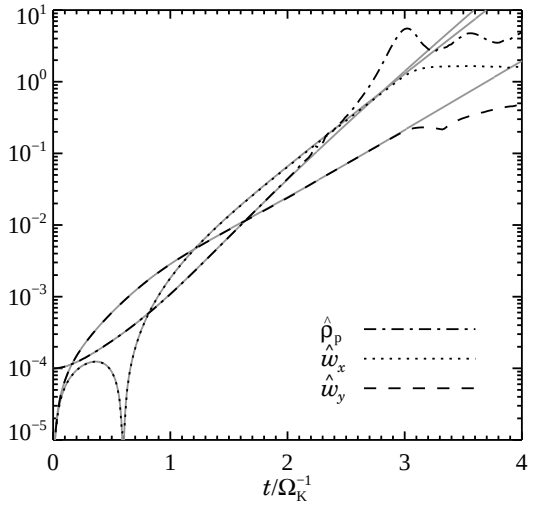

Figure 1: The evolution of a self-gravitating shear wave of solid particles. The plot shows a comparison between the semi-analytic solution to the linearised equation system (grey lines) and the solution obtained with the full solver of the Pencil Code (dark dotted, dashed and dot-dashed lines) for the amplitude of the particle density $\hat{\rho}_\mathrm{p}$ and of the particle velocity components $\hat{w}_x$ and $\hat{w}_y$. There is excellent agreement between the numerical and the analytical solutions in the entire linear range. After $\hat{\rho}_\mathrm{p} \sim 0.1$ the analytical solution is no longer valid and the two solutions diverge.

We show the evolution of the analytical solution and of the solution obtained with the Pencil Code in Fig. 1. There is an excellent agreement between the two solutions up to around $\hat{\rho}_\mathrm{p} = 0.1$ where the problem enters the nonlinear regime and the analytical solution loses its validity (but the Pencil Code solution does not).

Next we derive an analytical solution to a fully non-linear one-dimensional gravitational collapse problem, following Spitzer[44], to test the Poisson solver outside the linear regime.

Consider the equation system governing a self-gravitating gas in an infinitely extended one-dimensional space along the z-axis:

$$\frac{\partial u_z}{\partial t} + u_z \frac{\partial u_z}{\partial z} = -\frac{\partial \Phi}{\partial z} - c_\mathrm{s}^2 \frac{\partial \ln \rho}{\partial z}\,, \tag{29}$$

$$\frac{\partial \ln \rho}{\partial t} + u_z \frac{\partial \ln \rho}{\partial z} = -\frac{\partial u_z}{\partial z}\,, \tag{30}$$

$$\frac{\partial^2 \Phi}{\partial z^2} = 4\pi G \rho\,. \tag{31}$$

We search for stationary solutions with $\dot{u}_z = \dot{\rho} = u_z = 0$. This yields a second order differential equation in ρ,

$$c_\mathrm{s}^2 \frac{\partial^2 \ln \rho}{\partial z^2} + 4\pi G \rho = 0\,. \tag{32}$$

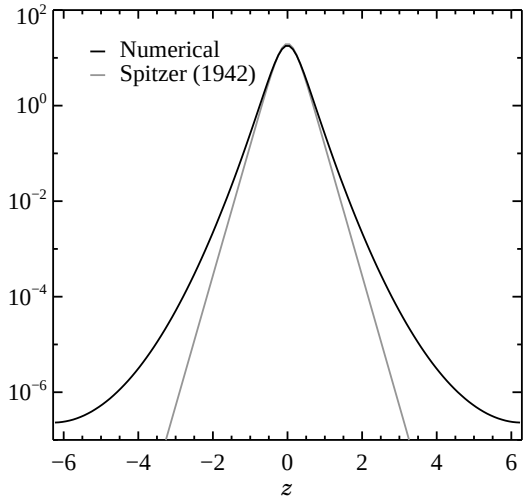

Figure 2: Comparison of numerical and analytical solution to the Spitzer[44] one-dimensional, non-linear collapse problem. The agreement is very good in high density regions, but there is disagreement in the underdense regions because the analytical solution assumes infinite space rather than a periodic domain.

The general solution is

$$\rho(z) = \frac{C_1 c_{\rm s}^2}{8\pi G}\left[1 - \tanh\left(\frac{1}{2}\sqrt{C_1}|z - z_0|\right)^2\right] \tag{33}$$

where

$$C_1 = \left(\frac{2\pi G \Sigma_{\rm g}}{c_{\rm s}^2}\right)^2 \tag{34}$$

is given by the column density of the gas and z_0 is an arbitrary constant. This is an exact solution to the full non-linear equation system and thus complements the linear test problem described in the previous section. We let the Pencil Code start with a Jeans unstable mode of wavenumber $k_z = 0.5$ in a periodic z-space of length $L_z = 4\pi$ covered by 64 grid points (we used shock viscosity to keep the code stable during the initial collapse). We show in Fig. 2 a comparison between the equilibrium state found by direct time integration of the equation system by the Pencil Code and the analytical equilibrium solution. There is an excellent agreement between the two solutions in regions of high and moderate density, whereas the underdense regions contain too much mass in the Pencil Code solution. This is however just an artefact of the comparison: the analytical solution works in infinitely extended space, whereas we assumed periodic boundary conditions in the numerical solution.

1.4 Collisional cooling

In the models that include collisional cooling we let unresolved collisions damp the velocity dispersion of the particles within each grid cell. The friction time in the Epstein[45] regime is

$$\tau_{\rm f} = \frac{a_\bullet \rho_\bullet}{c_{\rm s} \rho_{\rm g}} \,, \tag{35}$$

where we follow the nomenclature of equation (4). The collisional time-scale is assumed to follow a simple scaling with the Epstein friction time,

$$\rho_{\rm g} c_{\rm s} \tau_{\rm f} = \rho_{\rm p} c_{\rm p} \tau_{\rm coll} \,, \tag{36}$$

where $\rho_{\rm p}$ is the bulk mass density of solids and $c_{\rm p}$ is the velocity dispersion of the boulders in a grid cell. We ignore for simplicity any proportionality factors of order unity (for the complete analytical expression of the cooling time-scale, see Garzó & Dufty[46]). If particles are in the Stokes drag regime rather than Epstein (see §1.2.2), then the collisional cooling time-scale actually decreases relative to the friction time, but for simplicity we do not model this regime here. Equation (36) allows us to calculate the collisional time-scale from the friction time as

$$\tau_{\rm coll} = \frac{\tau_{\rm f}}{(c_{\rm p}/c_{\rm s})(\rho_{\rm p}/\rho_{\rm g})} \,, \tag{37}$$

without any reference to the radius and solid density of the particles. We discuss below how this expression changes when particles of several sizes collide.

Taking a velocity dispersion of $c_{\rm p}/c_{\rm s} \sim 1 \times 10^{-2}$ for the random motion of particles within a grid cell gives a threshold solids-to-gas ratio of $\epsilon \sim 100$ where collisions between boulders becomes as important as collisions between boulders and gas molecules. The collisional cooling is implemented as a simple term that reduces the velocity of a particle relative to the mean velocity of the particles in a grid cell on a collisional time-scale,

$$\frac{\partial \boldsymbol{v}^{(i)}}{\partial t} = -\frac{1 - C_{\rm res}}{\tau_{\rm coll}} (\boldsymbol{v}^{(i)} - \overline{\boldsymbol{v}}^{(\boldsymbol{k})}) \,, \tag{38}$$

where $\overline{\boldsymbol{v}}^{(\boldsymbol{k})}$ is the average particle velocity in cell $\boldsymbol{k}$ in which particle i is situated. The coefficient of restitution $C_{\rm res}$ is a measure of the degree of energy conservation in the impacts. We take $C_{\rm res} = 0.1$, corresponding to a loss of 90% of the relative velocity in each collision, a reasonable value for collisions between macroscopic solids[47], giving a collisional cooling time-scale that is approximately the same as the collisional time-scale

For collisions between particles of multiple sizes we replace equation (37) with the equation

$$\tau_{\rm coll} = \frac{\tau_{\rm f}^*}{(c_{\rm p}/c_{\rm s}) \sum_i (\rho_i/\rho_{\rm g})} \,, \tag{39}$$

where ρ_i is the local bulk density of solids of species i. The size-modified friction time $\tau_{\rm f}^*$ is an average of the friction times of the individual species weighted with the local bulk density of the individual species,

$$\tau_{\rm f}^* = \frac{\sum_i (\rho_i/\rho_{\rm g})}{\sum_i (\rho_i/\rho_{\rm g}) \tau_i^{-1}} \,. \tag{40}$$

Using $\tau_{\rm f}^*$ as the effective friction time, we can define a single cooling time-scale for all particle size bins. This ensures that the parameterised collisional cooling conserves momentum. For a single particle size the effective friction time reduces to the friction time, $\tau_{\rm f}^* = \tau_{\rm f}$.

In the numerical simulations we calculate the collision speed of particles in a given grid cell i by first calculating the mean velocity in the cell $\overline{\boldsymbol{v}}^{(i)}$. We then calculate the average particle collision speed as

$$c_{\rm p}^{(i)} = \overline{|\boldsymbol{v}^{(i)} - \overline{\boldsymbol{v}}^{(i)}|}\,. \tag{41}$$

This value is then plugged into equation (37) to get the collisional time-scale. This approach must be taken when using superparticles, as collisions cannot directly be followed as could, in principle, be done for individual particles.

1.5 Initial condition

Our simulations are initialised with a uniform density gas, $\rho_{\rm g} = 1$, with isothermal sound speed $c_s = 1$. The superparticles are randomly distributed in space, and the mass of each superparticle is set such that the column density of solids is $\Sigma_{\rm p} = 0.01\sqrt{2\pi}H\rho_{\rm g,mid}$. Here we have assumed that prior to the start of the simulation, sufficient sedimentation has occurred to bring all the solids within the computational domain. The particles are given random velocities with a Gaussian distribution of width $\delta v = 1 \times 10^{-3} c_{\rm s}$. The domain is cubic with $L_x = L_y = L_z = 1.32H$, where H is the pressure scale height of the disc. We use periodic boundary conditions in the azimuthal y-direction and in the vertical z-direction and shearing periodic boundary conditions in the radial x-direction[48]. The Keplerian rotation frequency at the central radius of the grid is $\Omega_{\rm K} = 1$. Assuming an orbital distance of $r = 5\,{\rm AU}$, a gas column density of $\Sigma_{\rm g} = 300\,{\rm g\,cm^{-2}}$ and a scale-height-to-radius ratio of $H/r = 0.04$ then gives $H = 3 \times 10^{12}\,{\rm cm}$, $\rho_{\rm g} = 4 \times 10^{-11}\,{\rm g\,cm^{-3}}$ and $c_{\rm s} = 500\,{\rm m\,s^{-1}}$ as physical properties of the disc. The column density of solids is $\Sigma_{\rm p} = 3\,{\rm g\,cm^{-2}}$ for a global solids-to-gas ratio of $\epsilon_0 = 0.01$.

1.5.1 Radial pressure support

The assumed radial pressure gradient, $\partial \ln P / \partial \ln r$, causes radial drift of the boulders following the expression[39]

$$v_x = \frac{(\partial \ln P/\partial \ln r)(H/r)}{\Omega_{\rm K}\tau_{\rm f} + (\Omega_{\rm K}\tau_{\rm f})^{-1}} c_{\rm s} = \frac{2\Delta v}{\Omega_{\rm K}\tau_{\rm f} + (\Omega_{\rm K}\tau_{\rm f})^{-1}} \tag{42}$$

in the absence of collective drag force effects on the gas (i.e. vanishing solids-to-gas ratio). With $(\partial \ln P/\partial \ln r)(H/r) = -0.04$ this gives $v_x = \Delta v = -0.02 c_{\rm s}$ for marginally coupled boulders with $\Omega_{\rm K}\tau_{\rm f} = 1$. We show in §1.14 the effect of less and more radial pressure support.

1.5.2 Magnetic fields

The Pencil Code solves the induction equation for the magnetic vector potential $\boldsymbol{A}$, keeping the magnetic field $\boldsymbol{B} = \boldsymbol{\nabla} \times \boldsymbol{A}$ solenoidal (i.e. $\boldsymbol{\nabla} \cdot \boldsymbol{B} = 0$) per construction. We initialise

magnetic fields by setting the initial vector potential

$$\boldsymbol{A} = A_0 \cos\left(\frac{2\pi}{L_x}x\right)\cos\left(\frac{2\pi}{L_y}y\right)\cos\left(\frac{2\pi}{L_z}z\right)\hat{\boldsymbol{y}}, \tag{43}$$

with $A_0 = 0.04$, which leads to an initial zero-net flux field with a maximum thermal to magnetic pressure ratio $\beta \simeq 55$. For the 256^3 run we add a very weak external vertical magnetic field of constant $\beta_{\rm ext} = 2 \times 10^5$. We found this latter field to be necessary to maintain a constant turbulent viscosity of $\alpha = 10^{-3}$ throughout the simulation.

1.5.3 Disc mass

We set for the 256^3 self-gravity simulation presented in the main text a value of $\tilde{G} = 0.1$, corresponding to a disc with Toomre[43] parameter $Q \approx 16$, an order of magnitude below the limit for global gravitational instability of the gas at $\tilde{G} = 1$ (at very large scales in an infinitely extended disc). For this reason we do not let the gas feel self-gravity, nor do we let the gas contribute to the gravitational potential in which the particles move. We have performed simulations that included the self-gravity of the gas, but found no significant gas overdensity in the gravitationally contracting particle clusters, due to the strong pressure support of the gas. Our choice of $\tilde{G}$ gives a gas surface density of $\Sigma_{\rm g} = 300\,{\rm g\,cm^{-2}}$ at $r = 5\,{\rm AU}$ (see eq. 20), approximately two times the minimum mass solar nebula (MMSN[38]). With moderate radial pressure support $\Delta v = -0.05 c_{\rm s}$ the column density limit is twice as high as for $\Delta v = -0.02 c_{\rm s}$, see §1.14. These are not unrealistic values for the actual column density of gas in the solar nebula, since the MMSN is a very conservative estimate of the column density that is calculated by adding up the heavy elements in the present Solar System and then dividing by the assumed interstellar solids-to-gas ratio. Any loss of material that occurred due to radial drift will then lead to an underestimate of the actual column density. Radial drift can also enhance the solids-to-gas ratio in the inner 10 AU by as much as an order of magnitude[49,6,50].

1.5.4 Particle sizes

We assume in all the models described here a global solids-to-gas ratio of $\epsilon_0 = 0.01$. There may be twice as much solid material present due to the condensation of volatiles into ice beyond the snow line at a few AU from the protostar. Coagulation models generally yield a particle mass distribution that spans two orders of magnitude in radius[28,27]. Our particle size distribution has size bin boundaries spanning an order of magnitude from $\Omega_{\rm K}\tau_{\rm f} = 0.125$ to $\Omega_{\rm K}\tau_{\rm f} = 1.125$. The assumption is then that the simulated boulders represent the upper half of the actual size range and that the lower half is present in smaller particles that are not effectively concentrated by transient high pressures and streaming instability and also are unable to participate in the collapse due to their strong coupling to the gas.

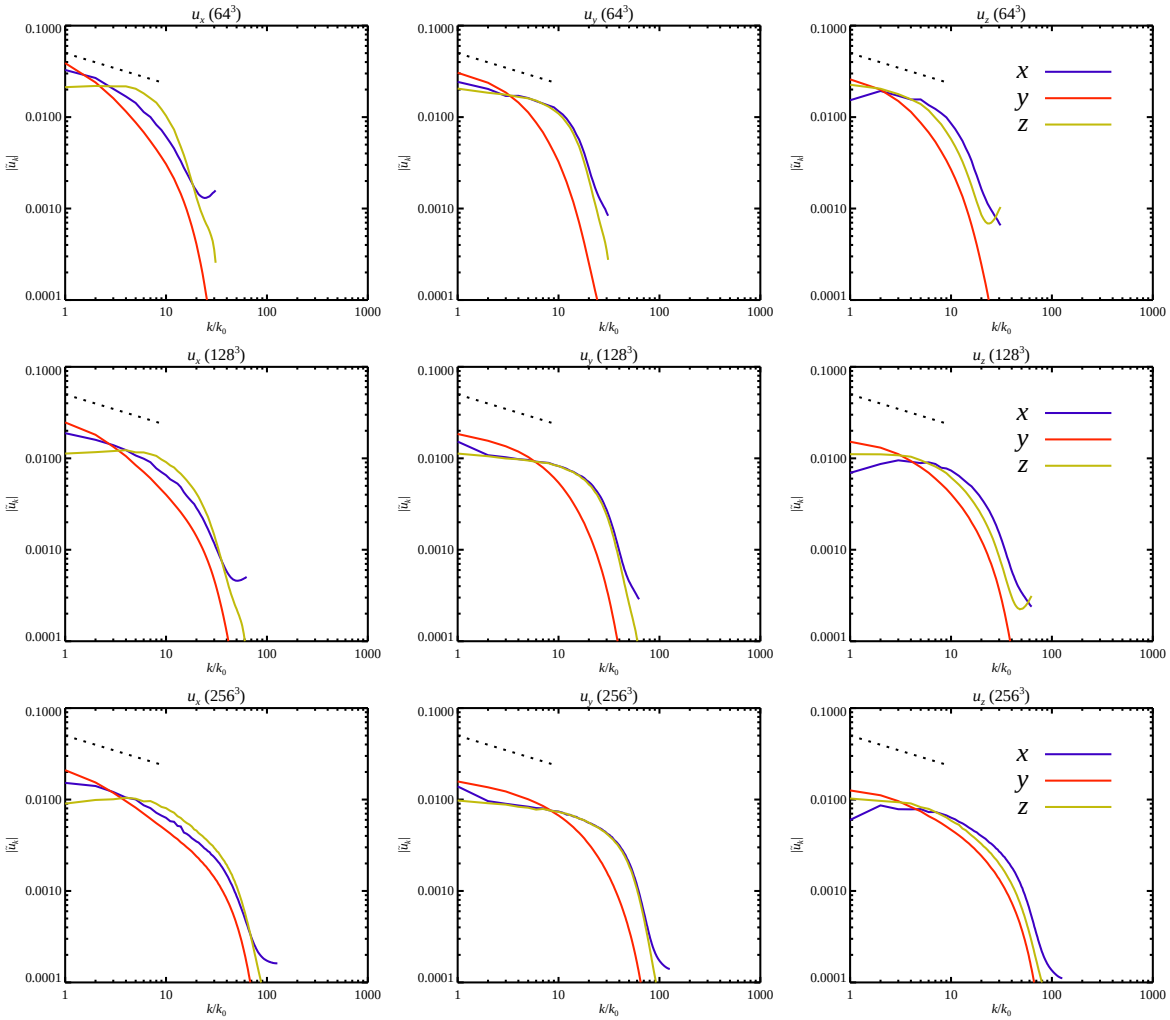

Figure 3: 1-D spectra of the gas velocity components with three different resolutions along the rows, the three different velocity components along the columns, and spectra taken in three different directions shown in each panel, in simulations with no particles. The different colours show power along the three coordinate directions, while the dotted line indicates a $k^{-1/3}$ Kolmogorov law.

1.6 Resolution study

1.6.1 Power spectra

Magnetorotational turbulence is known to produce a Kolmogorov-like power spectrum[48] with velocity amplitude on scale k going as $u_k \propto k^{-1/3}$ in the inertial range where numerical viscosity is insignificant. Increasing resolution leads to an increase in the inertial range. We show in Fig. 3 the modulus of the velocity amplitude as a function of wavenumber k normalised with the wavenumber of the largest scale of the box. A Kolmogorov $k^{-1/3}$ power

Resolution	$N_{\rm par}/10^6$	$\Delta t_{\rm grav}$	α
(1)	(2)	(3)	(4)
64^3	0.125	10.0	0.002
128^3	1.0	7.0	0.001

Resolution	$\tilde{G}$	Q	$N_{\rm clusters}$	$\dot{M}_{\rm cluster}$	$\dot{M}_{\rm cluster}/\tilde{G}_{0.1}$	M_4
(5)	(6)	(7)	(8)	(9)	(10)	(11)
64^3	0.4	4.0	2	7.5	1.9	42
128^3	0.4	4.0	4	2.9	0.7	65

Table 1: Resolution study for fixed $\tilde{G}$. Col. (1): Mesh resolution. Col. (2): Number of superparticles in millions. Col. (3): Number of orbits with self-gravity. Col. (4): Measured turbulent viscosity. Col. (6): Self-gravity parameter. Col. (7): Corresponding Toomre $Q \approx 1.6\tilde{G}^{-1}$. Col. (8): Number of clusters at the end of the simulation. Col. (9): Accretion rate of the most massive cluster in Ceres masses per orbit. Col. (10): Accretion rate normalised with $\tilde{G}_{0.1} \equiv \tilde{G}/0.1$. Col. (11): Total mass in the four most massive gravitationally bound clusters at 7 orbits after self-gravity is turned on.

law is indicated with a dotted line for reference. The turbulence is notably weaker in the z-direction than in the x- and y-directions. It also clear from Fig. 3 that the inertial range expands as expected with increasing resolution. Resolving the turbulent scales is important for resolving the local velocity dispersion ("temperature") of the particles and thus for the gravitational collapse (see §1.11).

1.6.2 Accretion

We check the convergence of the accreted mass using runs described in Table 1. We compare runs at 64^3 and 128^3 zone resolution, using a column density (parameterised by the self-gravity parameter $\tilde{G}$) that allows the 64^3 simulation to undergo gravitational collapse into discrete clusters. We find that the 128^3 run forms four clusters while the 64^3 run only forms two. However, the most massive cluster accretes faster in the low resolution case, because it does not have to compete for particles with other clusters. In Fig. 4 we plot the mass in the four most massive clusters as a function of time. The clusters in the 128^3 run accrete at approximately 50% higher rate than in the 64^3 run, because there are more clusters upon which particles can accrete. This is also evident from the last column of Table 1 where we write the total mass of the four most massive, bound clusters at a time of 7 orbits after self-gravity is turned on. In Fig. 5 we plot the maximum bulk density of particles and the mass of the most massive bound cluster as a function of time (similar to Fig. 3 of the main text). It is clear that the most massive cluster contains more mass and accretes faster in the 64^3 simulation. At the same time the maximum density is higher in the 128^3 simulation, because the increased resolution leads to less smoothing in the particle-mesh scheme (see §1.2).

We emphasise that the gravitational collapse of overdense seeds in turbulence is inherently a stochastic process, because of the temporal variability of the overdensities, so that convergence is not expected in the strict meaning of the term. Only convergence to mean values can be

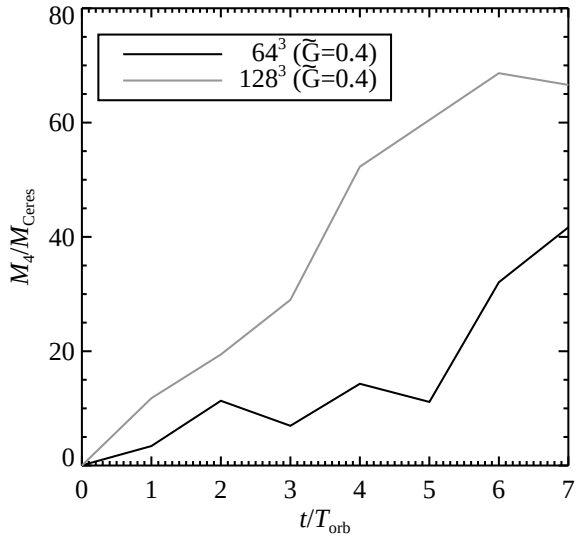

Figure 4: Total mass in the four most massive gravitationally bound clusters, in units of Ceres masses, plotted versus time since self-gravity was turned on, for two resolutions but a fixed self-gravity parameter $\tilde{G}$ that allows gravitational collapse at both 64^3 and at 128^3. The higher resolution run accretes at a 50% higher rate onto four clusters condensed out of the midplane layer, while only two clusters formed in the 64^3 run.

expected over a large ensemble of simulations. The limited number of tests that we have been able to perform within available computational resources should therefore be taken as qualitatively suggestive rather than conclusive.

1.6.3 Gravitational collapse

We have also done a resolution study of the column density required for gravitational collapse of the particle layer to occur, with results given in Table 2. The midplane layer in all runs presented here is resolved with an initial average of around four particles per grid cell, enough for the TSC scheme to define meaningful particle densities for the self-gravity solver. Collapsing regions have many more particles in each cell, of course. The column density limit for forming gravitationally bound clusters (see column 6 of Table 2) decreases with increasing grid resolution at all resolutions we have been able to study to date, as determined by varying the column density in increments of $\Delta\Sigma_{\rm g} = 300$ g cm^{-3}, equivalent to $\Delta\tilde{G} = 0.1$.

The observed decrease in limiting column density appears to be partly because of a decrease in the strength of the magnetorotational turbulence with increasing resolution, at least at lower resolution. The strength of the turbulence can be parameterised by the effective turbulent viscosity, which drops from $\alpha = 0.002$ at 64^3 to $\alpha = 0.001$ at 128^3 and 256^3, allowing a slightly denser midplane layer to form.

A more important factor, though, is that the particle density field becomes better resolved on

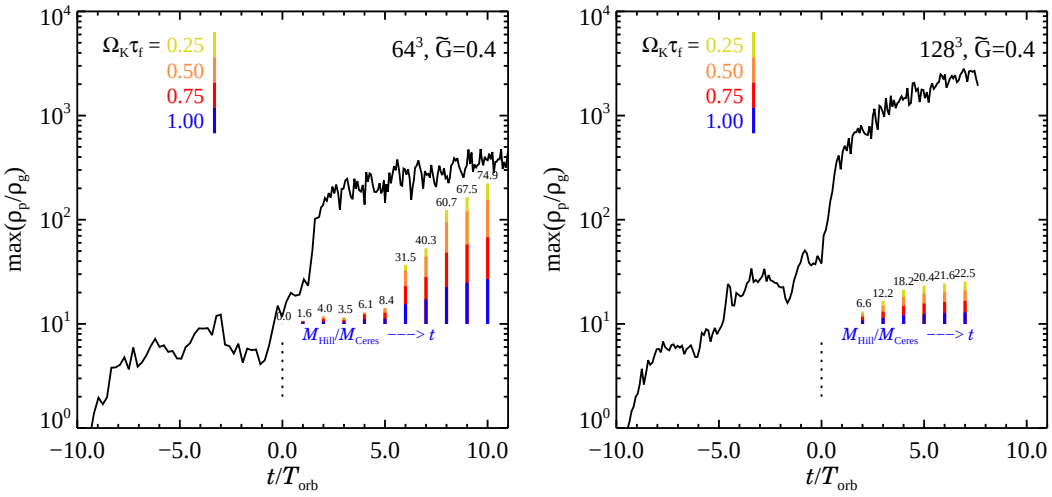

Figure 5: The maximum bulk solid density and the mass of the most massive bound cluster as a function of time for a fixed value $\tilde{G} = 0.4$ at 64^3 (left, 1.25×10^5 particles) and at 128^3 (right, 1×10^6 particles). The 64^3 run produces only 2 clusters (see Table 1), but the most massive one accretes lots of solid material (7.5 $M_{\rm Ceres}$ per orbit), whereas at the increased resolution of 128^3 four clusters form and they must compete for particles to accrete, thus the accretion rate of the most massive cluster decreases. The maximum bulk density of particles increases for higher resolution because the particle density field is better resolved by the TSC assignment scheme (see §1.2). Fig. 4 shows that the *total* mass accretion onto bound clusters in the 128^3 simulation is actually twice as high as in the 64^3 simulation.

the grid at higher resolution. The TSC assignment scheme underestimates the amplitude of density modes with wavelength near the grid size[19], so the self-gravity solver underestimates the gravitational acceleration caused by structures at those small scales. This can be seen in Fig. 6, where we show the maximum particle density produced by streaming instability and concentration in transient high pressures in models with neither self-gravity nor collisional cooling. Increasing linear resolution by a factor of two increases maximum density by around a factor four. Thus only higher resolution models reach the Toomre criterion for collapse at low column densities.

We write in columns 12 and 13 of Table 2 the mass in the four most massive, bound clusters and the same parameter divided by $\tilde{G}_{0.1} \equiv \tilde{G}/0.1$. There is less (normalised) mass accretion at 256^3 than at lower resolutions. This is readily explained because collapse can take place in smaller regions when the resolution is increased. The clusters thus contain less mass and accrete slower, at least to begin with, although the 256^3 has not run long enough to reveal the behaviour over longer times.

Another important effect is the resolution of the initial gravitational contraction. Fig. 2 in the main text shows that self-gravity results first in a radial contraction of the overdense seed bands. This contraction continues until the bands reach the Hill density where self-gravity dominates over tidal force, allowing a full non-axisymmetric collapse into bound clusters occurs. However, the self-gravity solver cannot follow collapse below a few grid cells, setting a

Resolution	$N_{\rm par}/10^6$	$\Delta t_{\rm grav}$	α
(1)	(2)	(3)	(4)
64^3	0.125	10.0	0.002
128^3	1.0	10.0	0.001
256^3	8.0	7.0	0.001

Resolution	$\tilde{G}$	Q	$\tilde{G}^{\rm (no\ coll)}$	$N_{\rm clusters}$	$\dot{M}_{\rm cluster}$	$\dot{M}_{\rm cluster}/\tilde{G}_{0.1}$	M_4	$M_4/\tilde{G}_{0.1}$
(5)	(6)	(7)	(8)	(9)	(10)	(11)	(12)	(13)
64^3	0.4	4.0	0.4	2	7.5	1.9	42	10.5
128^3	0.2	8.0	0.3	2	1.8	0.9	19	9.5
256^3	0.1	16.0	–	4	0.5	0.5	6	6

Table 2: Resolution study for gravitational collapse. Col. (1): Mesh resolution. Col. (2): Number of superparticles in millions. Col. (3): Number of orbits with self-gravity. Col. (4): Measured turbulent viscosity. Col. (6): Minimum self-gravity parameter where gravitationally bound clusters form (MMSN has $\tilde{G} \approx 0.05$ at $r = 5$ AU). Col. (7): Corresponding Toomre $Q \approx 1.6\tilde{G}^{-1}$. Col. (8): Minimum self-gravity parameter where gravitationally bound clusters form without collisional cooling. Col. (9): Number of clusters at the end of the simulation. Col. (10): Accretion rate of the most massive cluster in Ceres masses per orbit. Col. (11): Accretion rate normalised with $\tilde{G}_{0.1} \equiv \tilde{G}/0.1$. Col. (12): Total mass in the four most massive gravitationally bound clusters at 7 orbits after self-gravity is turned on. Col. (13): Total cluster mass normalised with $\tilde{G}_{0.1} \equiv \tilde{G}/0.1$.

resolution-dependent minimum width on the radial bands. Increasing the resolution decreases the final width of the bands, increasing their density, and thus allowing full collapse to occur in models with lower initial column densities. After collapse sets in, higher resolution allows collapse to higher densities, again resulting in higher peak densities in higher resolution models.

Poisson noise due to the discrete nature of the superparticles on the other hand, appears to be quite insignificant for gravitational collapse. We have done tests with particle numbers as high as thirty particles per cell (in the mid-plane layer) in the 64^3 runs (10^6 particles) and eight particles per cell in the 128^3 runs (2×10^6 particles) and found the column density for collapse to be unchanged from runs with the same grid resolution and only four particles per cell. The overdense seeds of the gravitational instability are under all circumstances resolved with several hundreds or thousands of particles, explaining this result.

Although we have clearly not yet obtained convergence in the gravitational collapse of the particles, the consistent trend towards higher peak densities and gravitational instability at lower average column density with increasing resolution lends strong support to our hypothesis that this mechanism can drive planetesimal formation at gas column densities characteristic of the minimum mass solar nebula.

To compensate for underresolving the peak densities, one could manually sharpen the underestimated density modes[19], but we prefer not to solve for the gravitational acceleration better than the pressure term, to avoid any risk of artificial fragmentation[51]. On the other hand, studies that use the adaptive mesh refinement method[52] in combination with a kinetic

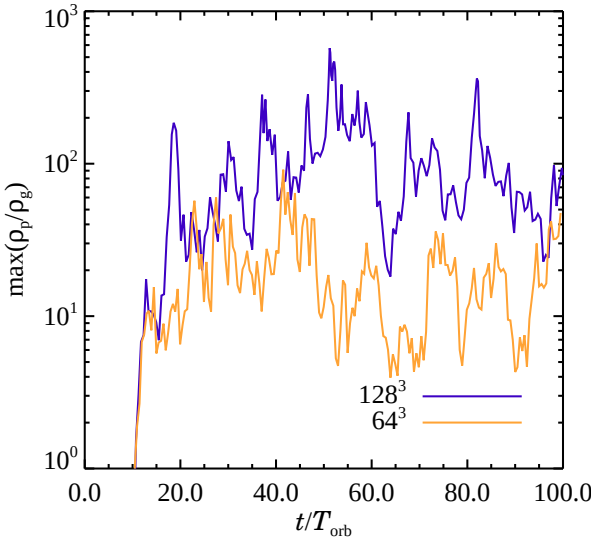

Figure 6: Maximum particle density on the grid, assigned from particle positions with the TSC scheme[19,37], versus time for runs with no self-gravity and no collisional cooling. The maximum density goes up by a factor of 3-4 for the 128^3 simulation, in part because the density field assigned with the TSC scheme on the grid has less smoothing at higher resolution.

particle code with collision detections[53] could be adapted to fully resolve the gas concentration of particles, and then follow the collapse and gravitational fragmentation of the boulder layer all the way up to solid density, allowing determination of the minimum column density for planetesimal formation and the final multiplicity of the self-gravitating boulder clusters that we model.

1.7 Collisional cooling

In the runs presented in the main text, we include the effect of collisional cooling on the collapse of the mid-plane layer into gravitationally bound clusters. However, the collisional cooling only marginally changes the column density at which collapse initially occurs. To demonstrate this, we have run simulations without collisional cooling to quantify its importance for gravitational collapse (see column 8 of Table 2). We show in Fig. 7 the maximum bulk density of solids in simulations with and without collisional cooling, for 64^3 (left plot) and 128^3 (right plot) grid simulations. At 64^3 resolution collapse occurs at $\tilde{G} = 0.4$ both with and without collisional cooling, although its inclusion seems to cause collapse to happen somewhat more quickly after self-gravity is turned on at $t = 0$. At a resolution of 128^3 zones, collapse occurs in the presence of collisional cooling at $\tilde{G} = 0.2$, whereas the column density limit without collisional cooling is roughly 50% higher. Collisional cooling is thus not a prerequisite of the collapse, but rather allows collapse to occur in somewhat lighter discs.

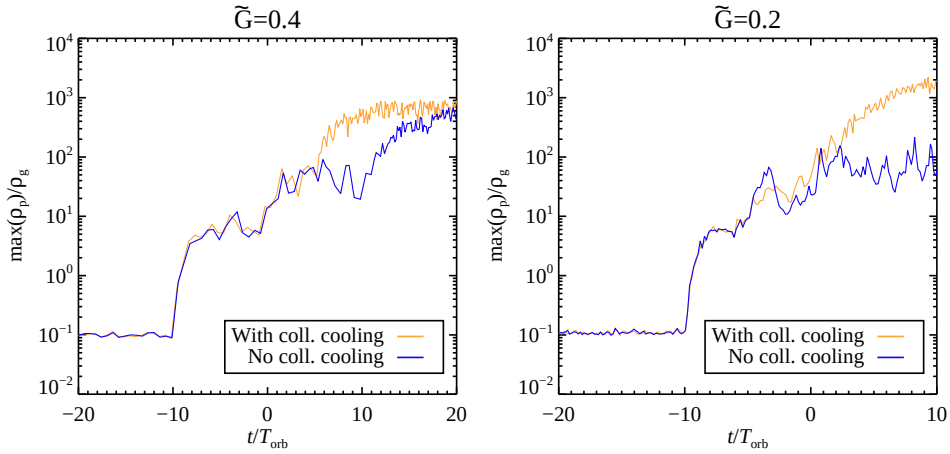

Figure 7: Comparison of runs with (bright/yellow) and without (dark/blue) collisional cooling (self-gravity and collisional cooling are turned on at $t = 0$). At 64^3 resolution, we find that collapse occurs at the same gas column density, independent of collisional cooling, although collisional cooling lets the collapse happen faster. At 128^3 collapse with collisional cooling occurs at $\tilde{G} = 0.2$, while $\tilde{G} = 0.3$ is needed when collisional cooling is not applied.

1.8 Jeans and Toomre criterion

The Jeans criterion[51,54] states that the local Jeans length for gravitational collapse of gas must be resolved by at least a few grid points, as otherwise artificial fragmentation may occur in marginally stable structures because of numerical discretisation errors. This is particularly a problem in the presence of rotation[54,55]. A corresponding Toomre[43] criterion[56] is appropriate for accretion discs. We show in §1.10 that the initial radial collapse phase is resolved by around 20 grid points, but gravitationally bound clusters eventually reach the size of a few grid cells, for which the unstable wavelengths that would lead to further fragmentation are not resolved. It is not snown whether artificial fragmentation is an issue for solid particles moving on a fixed mesh. The TSC scheme inherently smooths out small scale power in the assigned particle density[19,37] (see also §1.2), so the contribution of the small scales to the gravitational potential is underestimated, whereas the particle velocity dispersion that counteracts contraction is resolved equally well at all scales. It is thus more likely that our numerical scheme suppresses fragmentation at the small scales and at crude resolutions; this is also supported by the resolution tests where gravitational collapse occurs at lower column density in higher resolution models. We have no reason to believe that the collapse of the particle layer should stop anywhere near the grid scale: the velocity dispersion in the overdense clusters is around 1% of the sound speed, so the pressure support is negligible[9], and drag force and inelastic collisions are highly efficient at dissipating kinetic energy. Instead we consider the condensed particle clusters to be equivalent to (numerically expensive) sink particles, a good approximation as long as there is no feedback from the unresolved scales back to the large scales[57].

1.9 Gammie cut-off

Gammie[20] argues that one must exclude wave numbers above a limit from the solution to the Poisson equation in the shearing box in order to keep the gravitational acceleration approximately isotropic at small scales in the presence of shear. The cut-off is at $k_{\max} = \sqrt{2}k_{\rm Ny}$ where $k_{\rm Ny}$ is the Nyquist wavenumber. This cut-off has been applied in all our simulations. We have run test simulations without the cut-off and found no significant differences in the resulting gravitational fragmentation, probably because the TSC assignment scheme itself underestimates the potential at these small scales.

1.10 Size of the forming bodies

The linear stability analysis of Goldreich & Ward[5] gives the largest wavelength unstable to radial self-gravity as

$$\lambda_{\rm GW} = \frac{4\pi^2 G\Sigma_{\rm p}}{\Omega_{\rm K}^2}\,, \tag{44}$$

where G is the gravity constant, $\Sigma_{\rm p}$ is the column density of solids and $\Omega_{\rm K}$ is the Keplerian orbital frequency. This expression is formally valid in the limit of vanishing particle velocity dispersion and ignores the potentially important effect of drag forces on the collapse[42,58]. Inserting nominal values at $r = 5\,{\rm AU}$ in the protosolar nebula gives

$$\lambda_{\rm GW} \approx 1.4 \times 10^{10}\,{\rm cm} \left(\frac{M_\star}{M_\odot}\right)^{-1} \left(\frac{\Sigma_{\rm p}}{1.5\,{\rm g\,cm^{-2}}}\right) \left(\frac{r}{5\,{\rm AU}}\right)^3 . \tag{45}$$

Using a scale height of $H = 3 \times 10^{12}\,{\rm cm}$ (see §1.5) and $\Sigma_{\rm p} = 15\,{\rm g\,cm^{-2}}$ in the radial overdensities of our simulations yields $\lambda_{\rm GW}/H \approx 0.1$, which is initially well-resolved (the grid size is $\delta x = \delta y = \delta z = 0.005H$ in the 256^3 simulation). Assuming that all the solid mass within a single unstable wavelength collapses to a gravitationally bound solid object, the radius of the object is

$$R \approx \left(\frac{\Sigma_{\rm p}\xi^2\lambda_{\rm GW}^2}{\rho_\bullet}\right)^{1/3} \approx 50\,{\rm km}\,\xi^{2/3} \left(\frac{M_\star}{M_\odot}\right)^{-2/3} \left(\frac{\Sigma_{\rm p}}{1.5\,{\rm g\,cm^{-2}}}\right) \left(\frac{r}{5\,{\rm AU}}\right)^2 \left(\frac{\rho_\bullet}{2\,{\rm g\,cm^{-3}}}\right)^{-1/3} , \tag{46}$$

where $\xi < 1$ is a parametrisation of the most unstable wavelength relative to the largest unstable wavelength. A reasonable value is $\xi = 1/2$.

At $r = 1\,{\rm AU}$ with $\Sigma_{\rm p} = 15\,{\rm g\,cm^{-2}}$ one recovers the 10 km planetesimals found by Goldreich & Ward[5]. The size of planetesimals falls to less than 1 km if the velocity dispersion of the particles is included, but the derivation ignores the effect of drag forces on energy dissipation[59,60,42,58]. Considering, on the other hand, an orbital radius $r = 5\,{\rm AU}$, with $\Sigma_{\rm p} = 30\,{\rm g\,cm^{-2}}$ in the radial overdensities found in the current work, the planetesimals reach radii of around 600 km, because the unstable wavelengths contain far more mass. These sizes agree roughly with the results of our numerical models.

1.11 Collision speeds

We show in Fig. 8 the collision speeds between bodies of different sizes in a 128^3 simulation without self-gravity or collisional cooling (from a snapshot taken at $t = 20T_{\rm orb}$). We consider a million particles of four different particle sizes at the same time, $\Omega_{\rm K}\tau_{\rm f} = 0.25, 0.50, 0.75, 1.00$ and two values of the radial pressure support, $\Delta v = -0.05c_{\rm s}$ and $\Delta v = -0.02c_{\rm s}$.

We have considered collisions between all particles within the same grid cell by measuring the relative speed of every single pair of particles, giving $(1/2)N(N-1)$ unique collisions in a grid cell with N particles. We note that this may underestimate the actual rate of fast collisions since in reality high speed collisions would happen more frequently. We also note that grid points with many particles get a high weight in the overall picture, and if these very dense grid points have a lower collision speed due to feedback shielding from the gas (see Figs. 13 and 14), this will also lead to a generally lower collision speed. All collisions were considered for simplicity to be head on. The more realistic case of random impact parameters would lead to a reduction of the measured collision speeds by more than 50%. We show for comparison the collision speeds measured at $t = 20T_{\rm orb}$ for 64^3 and 256^3 simulations in Figs. 9–10. For the 64^3 the Mach number of the gas is overall larger, Ma ≈ 0.07 compared to Ma ≈ 0.05 at 128^3, and collision speeds are also larger than in Fig. 8. There is very little difference between the 128^3 and the 256^3 collision speeds, but the data is based on only one snapshot. More statistically significant convergence tests, given in §1.11.1, show a slight increase in collision speeds (relative to large scale rms speeds) with increasing resolution.

Equal-sized bodies have no differential drift, so turbulent motions dominate the distribution of collision speeds, while differential drift (dotted lines in Fig. 8) dominates the distribution of collisions between bodies of different sizes.

Following Benz[3] we calculate the threshold for destructive collisions. We use the specific incoming kinetic energy

$$\mathcal{K} = (1/2)mv^2/M\,, \tag{47}$$

where v is the collision speed and m and M are the impactor and target mass, respectively, with $M > m$. Collisional fragmentation occurs at a limit $\mathcal{K}^\star \approx 3\times10^6\,{\rm erg\,g^{-1}}$ for metre-sized solid bodies and $\mathcal{K}^\star \approx 6\times10^5\,{\rm erg\,g^{-1}}$ for metre-sized rubble piles[3]. This allows us to calculate the destructive collision threshold from equation (47) for any pair of bodies (see Fig. 8). We have ignored any shape effects that could lead to differential drift of equal mass bodies[3]. More collisions exceed the destruction threshold for equal-sized bodies than other cases, but destructive collisions still only form a minority of the total, although the fraction of destructive collisions depends on poorly known material properties of the boulders. Note that our bodies are in fact smaller than the 1 m considered by Benz, so the destruction threshold speeds may in reality be higher since smaller bodies are expected to be able to withstand higher collision speeds. Higher radial pressure support does not produce markedly more collisional fragmentation, as can be seen by comparing the grey and dark lines in Fig. 8. The collisions for which the relative speed increases with the drift speed are between different-sized bodies, and those collisions can withstand much higher relative speeds, whereas higher radial pressure support does not give equal-sized bodies a higher collision speed. A third possibility for the internal makeup of the bodies is that they are icy, porous structures. It is shown by Ryan et al.[61] that such objects are generally as strong as the silicates considered by Benz[3]. We ignore

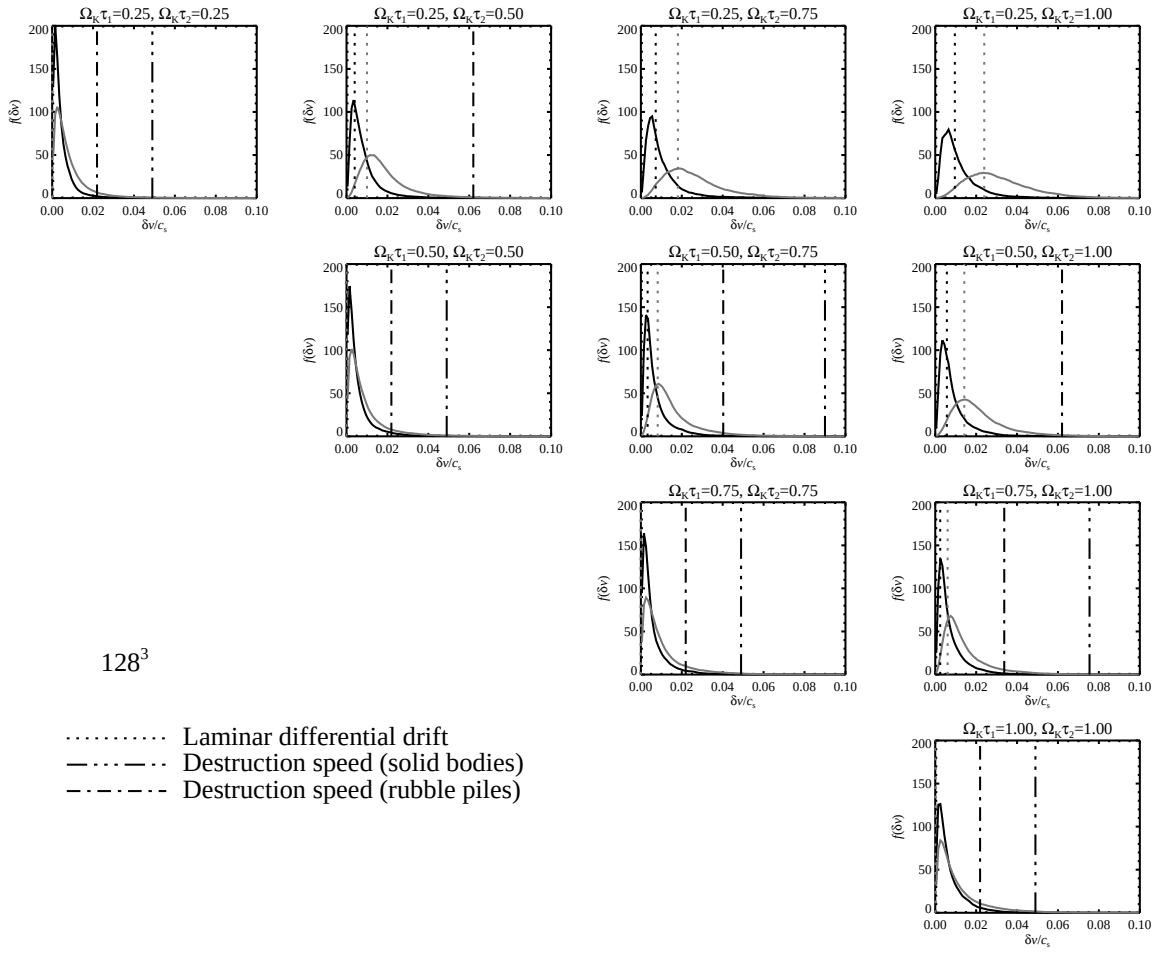

Figure 8: Distribution of collision speeds between boulders of different sizes for a radial pressure support of $\Delta v = -0.05 c_{\rm s}$ (grey line) and $\Delta v = -0.02 c_{\rm s}$ (dark line), both for 128^3 grid points and 1,000,000 particles *without* either collisional cooling or self-gravity. The laminar solution for the relative speed due to differential drift (in radial and azimuthal velocity) is shown with a dotted line (with an assumed solids-to-gas ratio of $\epsilon = 0.5$). This is the major contribution for different-sized bodies, whereas equal-sized bodies only obtain collision speed due to turbulent motions in the gas. The threshold for destruction is shown for solid bodies (dot-dot-dot-dashed line) and for rubble piles (dot-dashed line) following Benz[3]. Equal-sized bodies have the lowest destruction threshold, but that is still in the far wing of the collision distribution. Small bodies and large bodies can survive collisions at much higher speeds, sometimes even beyond the range shown along the δv axis (i.e. $> 0.1 c_{\rm s}$, where $c_{\rm s}$=500 m/s). The collision speed between equal-sized bodies is relatively unchanged when increasing the pressure support to $\Delta v = -0.05 c_{\rm s}$. The increased differential drift, however, manifests itself in higher collision speeds between different-sized bodies.

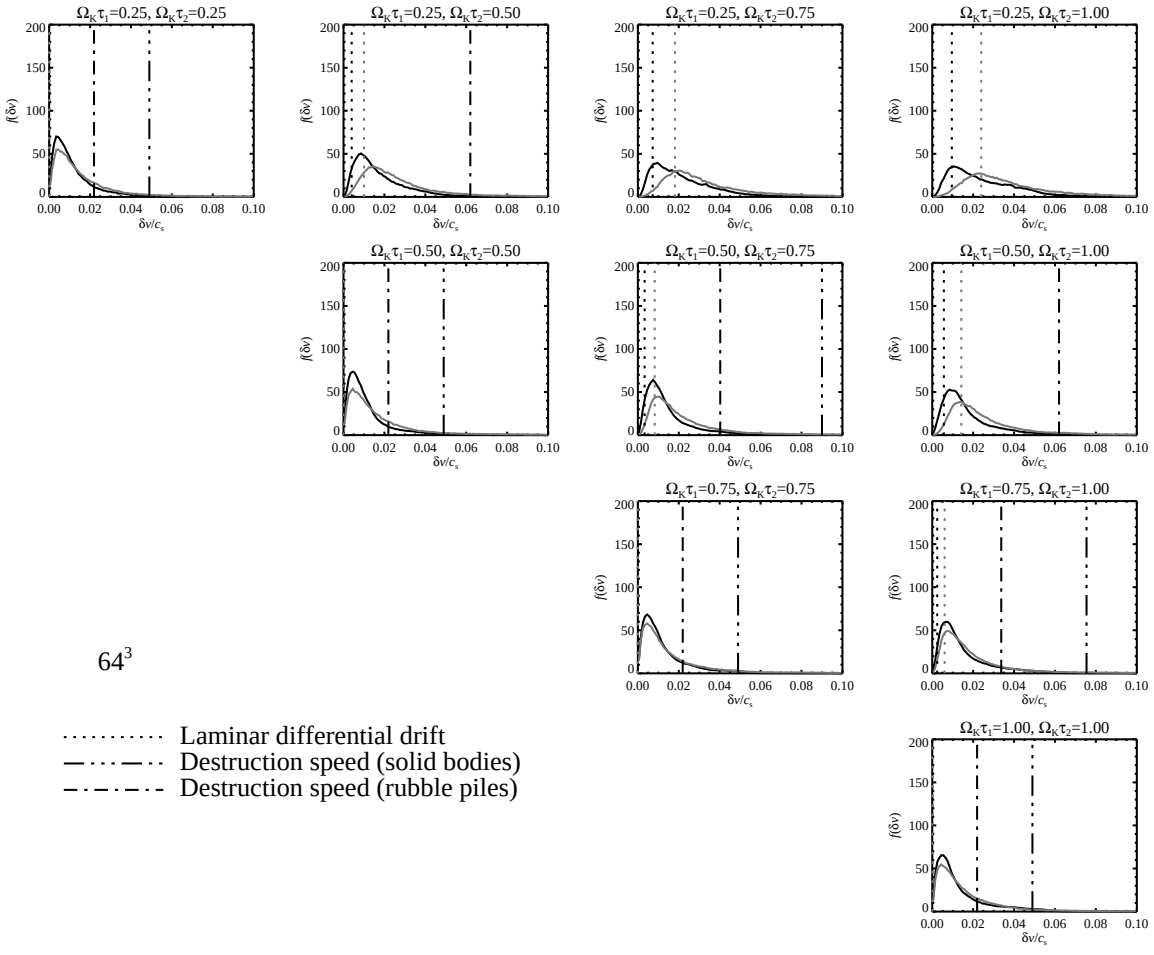

Figure 9: Same as Fig. 8, but for 64^3 grid points with 125,000 particles. The overall Mach number of the turbulent flow is 30-40% higher than in the higher resolution runs, hence collision speeds are somewhat higher.

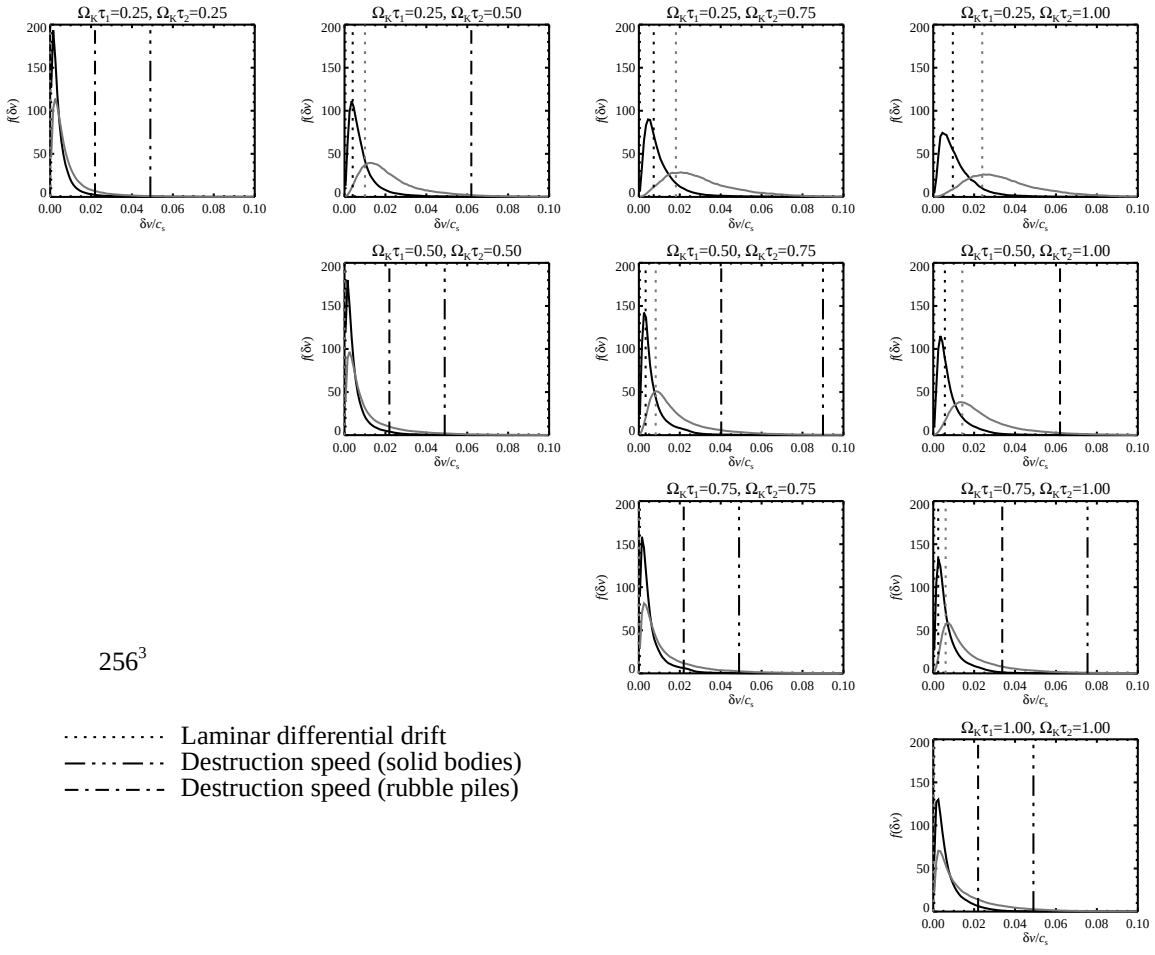

Figure 10: Same as Fig. 8, but for 256^3 grid points with 8,000,000 particles. Here we considered for simplicity only 1/8 of the immense amount of possible collisions. The collision speeds agree well with those of Fig. 8.

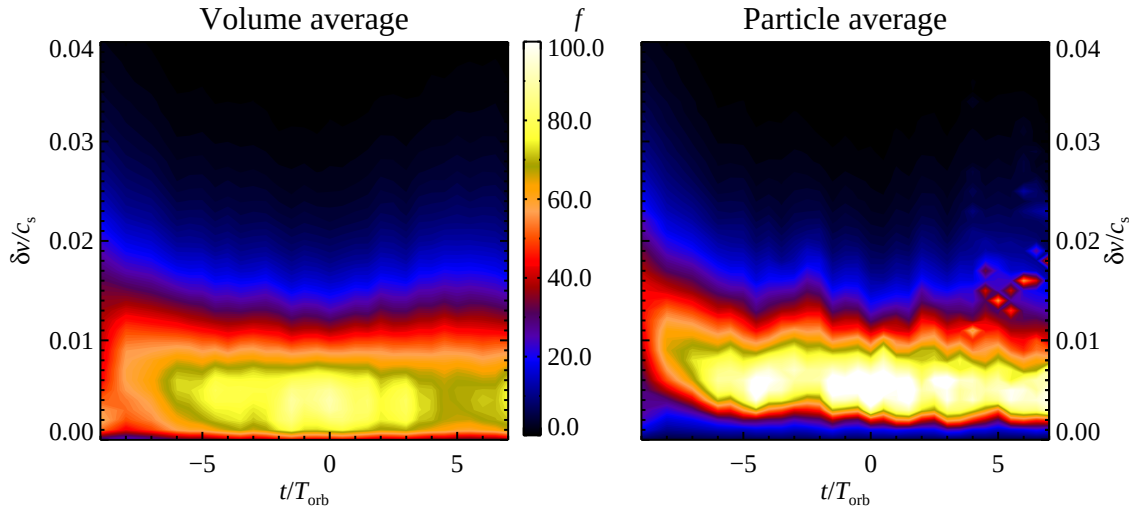

Figure 11: The distribution of particle collision speeds (volume average, left plot) in units of sound speed, also shown weighted with number of particles in the grid cell (particle average, right plot), for $\Delta v = -0.02 c_\mathrm{s}$ and four different particle sizes $\Omega_\mathrm{K} = 0.25, 0.50, 0.75, 1.00$. The distribution function f is normalised such that $\int_0^\infty f(t, \delta v) \mathrm{d}(\delta v / c_\mathrm{s}) = 1$ for all t. Collisional cooling and self-gravity are turned on at $t = 0$, halfway through these runs, with little effect on average collision speeds until late times. Collisional cooling is only efficient in the few regions where the solids-to-gas ratio is very high, so the average collision speeds are not much affected. Accretion onto the condensed out clusters is visible in the right panel at late times.

in the present analysis other effects of collisions, such as erosion that may deplete boulders of mass even if the collision speed is below the threshold for destruction.

A quite serious issue related to collisional fragmentation is that it could reduce the number of particles large enough to take part in gravitational collapse prior to the collapse to as little as 20% of the total mass of the solids[28,27]. This is particularly relevant in the inner solar nebula where the sound speed is high. In that case we speculate that an augmentation of the solids-to-gas ratio by up to a factor 5 would be needed for gravitational collapse to occur in the midplane layer. Note that we already assume that half of the solid mass is present in small grains too well-coupled to the gas to take place in the collapse (assuming that the total abundance of solids and ices is 0.017 times that of the gas[38]). A more detailed modelling of collisional fragmentation is needed to quantify its actual effect on the gravitational collapse.

We show in Fig. 11 the time evolution of the average collision speed of the particles for a radial pressure support of $\Delta v = -0.02 c_\mathrm{s}$. The volume average collision speed distribution has one speed associated with each grid cell whereas the particle average collision speed distribution has the local collision speed weighted by the number of particles in the grid cell. Collisional cooling, turned on together with self-gravity at $t = 0$ in Fig. 11, does not reduce collision speeds broadly, since only regions with very high solids-to-gas ratios have sufficiently high collision rates for cooling to be effective. Accretion with high relative speeds onto condensed clusters is visible at late times in the particle average distribution. Some of

the high-speed collisions that occur during the accretion phase, especially among boulders that have already been deformed in earlier collision events, may in reality lead to erosion or destruction of the colliding bodies[3]. However, the fragments remain within the Hill sphere of the gravitationally bound cluster, so their dynamics is dominated by the gravity of the nearby cluster rather than by the tidal force of the protostar. Furthermore, the mean free path of the fragments, $\ell/H \approx \Omega_{\rm K}\tau_{\rm f}/(\rho_{\rm p}/\rho_{\rm g}) \sim 10^{-3}$, is shorter than the size of the bound clusters, so they will undergo collisions with the remaining boulders, leading only to the further growth of the remaining boulders as they sweep up the fragments. All in all collisional destruction of boulders (or, rather, the lack of widespread collisional destruction) is important for obtaining an initial condition with a sufficient amount of the solid material bound in boulders, whereas collisional destruction during the gravitational collapse phase is probably only of secondary importance.

1.11.1 Comparison of rms and collision speeds with analytic values

We now aim to explain why the relative (i.e. collisional) speeds are only $\delta v \approx 0.01 c_{\rm s}$ for marginally coupled particles despite turbulent motions of Mach number $\mathcal{M} = u_{\rm t}/c_{\rm s} = 0.05$. We summarise the four main effects: (1) due to finite friction times particles are not fully accelerated by the turbulence, so rms particle speeds are reduced below that of the gas; (2) particle drag on gas tends to reduce both random and relative speeds; (3) particles are well enough coupled to eddies that collision speeds are slower than rms speeds due to entrainment by the same extended eddies; and (4) even though we have a fairly long inertial range in the 256^3 simulations, particles gain relative speed from scales near the onset of the dissipative subrange, so it is not certain that all the relevant scales are resolved. We present extensive documentation of effects (1) and (2) in this section, while point (4) is given some support by a 10-20% increase of collision speeds relative to rms speeds when going from 64^3 to 128^3 grid points (see Figure 16).

We emphasise that there is no complete theory describing all these effects, so the current numerical study deepens our understanding of these issues. Notably an analytical theory for collision speeds that includes orbital dynamics is, to our knowledge, missing (even without drag of particles on gas), so verification of point (3) above is difficult and the point is left as speculation in this work. We also emphasise that our results show that the collision speed increases slightly with increasing resolution and that higher resolution studies will be needed to see if the collision speeds have converged. The important issue of collision speeds of marginally coupled solids will need more consideration in the future.

First a word on nomenclature and on calculation procedure:

- With *rms speeds* we refer to the overall root-mean-square speed of either gas or particles. This value is directly obtained from calculating the root-mean-square of all values of a chosen component of gas or particle velocity.
- *Collision speed* refers to the local velocity differences of particles within a single grid cell (similar to the sound speed or mean thermal speed of the gas). We calculate the mean collision speed of particles by following 1000 particles from the greater ensemble and

Without feedback (128^3):

$\Omega_{\rm K}\tau_{\rm f}$	$\sigma_x^{(\rm p)}$	$\sigma_y^{(\rm p)}$	$\sigma_z^{(\rm p)}$	$\sigma_x^{(\rm g)}$	$\sigma_y^{(\rm g)}$	$\sigma_z^{(\rm g)}$	$\sigma_x^{(\rm p)}/\sigma_x^{(\rm g)}$	$\sigma_y^{(\rm p)}/\sigma_y^{(\rm g)}$	$\sigma_z^{(\rm p)}/\sigma_z^{(\rm g)}$
0.20	0.0307	0.0230	0.0205	0.0317	0.0294	0.0240	0.9686	0.7844	0.8515
0.50	0.0313	0.0191	0.0172	0.0321	0.0300	0.0244	0.9762	0.6367	0.7049
1.00	0.0305	0.0149	0.0138	0.0326	0.0300	0.0246	0.9353	0.4967	0.5599
2.00	0.0271	0.0120	0.0113	0.0331	0.0312	0.0251	0.8192	0.3834	0.4510
5.00	0.0186	0.0082	0.0074	0.0329	0.0311	0.0249	0.5644	0.2648	0.2961

Without feedback (64^3):

$\Omega_{\rm K}\tau_{\rm f}$	$\sigma_x^{(\rm p)}$	$\sigma_y^{(\rm p)}$	$\sigma_z^{(\rm p)}$	$\sigma_x^{(\rm g)}$	$\sigma_y^{(\rm g)}$	$\sigma_z^{(\rm g)}$	$\sigma_x^{(\rm p)}/\sigma_x^{(\rm g)}$	$\sigma_y^{(\rm p)}/\sigma_y^{(\rm g)}$	$\sigma_z^{(\rm p)}/\sigma_z^{(\rm g)}$
0.20	0.0428	0.0322	0.0289	0.0448	0.0422	0.0344	0.9554	0.7628	0.8394
0.50	0.0429	0.0263	0.0248	0.0448	0.0422	0.0344	0.9573	0.6234	0.7201
1.00	0.0404	0.0207	0.0198	0.0448	0.0422	0.0344	0.9019	0.4909	0.5764
2.00	0.0340	0.0161	0.0152	0.0448	0.0422	0.0344	0.7590	0.3815	0.4408
5.00	0.0237	0.0115	0.0104	0.0448	0.0422	0.0344	0.5283	0.2731	0.3025

With feedback (128^3):

$\Omega_{\rm K}\tau_{\rm f}$	$\sigma_x^{(\rm p)}$	$\sigma_y^{(\rm p)}$	$\sigma_z^{(\rm p)}$	$\sigma_x^{(\rm g)}$	$\sigma_y^{(\rm g)}$	$\sigma_z^{(\rm g)}$	$\sigma_x^{(\rm p)}/\sigma_x^{(\rm g)}$	$\sigma_y^{(\rm p)}/\sigma_y^{(\rm g)}$	$\sigma_z^{(\rm p)}/\sigma_z^{(\rm g)}$
0.20	0.0276	0.0194	0.0172	0.0318	0.0307	0.0244	0.8655	0.6315	0.7046
0.50	0.0279	0.0166	0.0150	0.0341	0.0341	0.0263	0.8199	0.4858	0.5698
1.00	0.0220	0.0111	0.0106	0.0337	0.0331	0.0257	0.6520	0.3350	0.4105

With feedback (64^3):

$\Omega_{\rm K}\tau_{\rm f}$	$\sigma_x^{(\rm p)}$	$\sigma_y^{(\rm p)}$	$\sigma_z^{(\rm p)}$	$\sigma_x^{(\rm g)}$	$\sigma_y^{(\rm g)}$	$\sigma_z^{(\rm g)}$	$\sigma_x^{(\rm p)}/\sigma_x^{(\rm g)}$	$\sigma_y^{(\rm p)}/\sigma_y^{(\rm g)}$	$\sigma_z^{(\rm p)}/\sigma_z^{(\rm g)}$
0.20	0.0423	0.0291	0.0265	0.0462	0.0434	0.0355	0.9147	0.6719	0.7450
0.50	0.0372	0.0224	0.0217	0.0479	0.0459	0.0363	0.7769	0.4881	0.5991
1.00	0.0388	0.0182	0.0184	0.0465	0.0432	0.0358	0.8335	0.4218	0.5134

Table 3: Particle and gas rms speeds and their ratios, for different values of the friction time. The top part of the table shows results for passive particles (i.e. with no friction force on the gas), whereas the bottom part shows the result when gas is allowed to feel friction. The gas Mach number is around Ma ≈ 0.05 for 128^3 grid points, while Ma ≈ 0.07 for 64^3 grid points. Small particles show the expected trend towards equal particle and gas rms speeds (the ratios are shown in the last three columns). The azimuthal particle rms speed falls quickly with increasing friction time as the loosely coupled particles go on elliptic orbits, and the ratio between radial and azimuthal particle rms speed approaches the expected value of 0.5. Particle rms speeds fall by a significant factor when gas is allowed to feel the friction from the particles – for $\Omega_{\rm K}\tau_{\rm f} = 1.0$ the reduction is around 25% when adding the components quadratically.

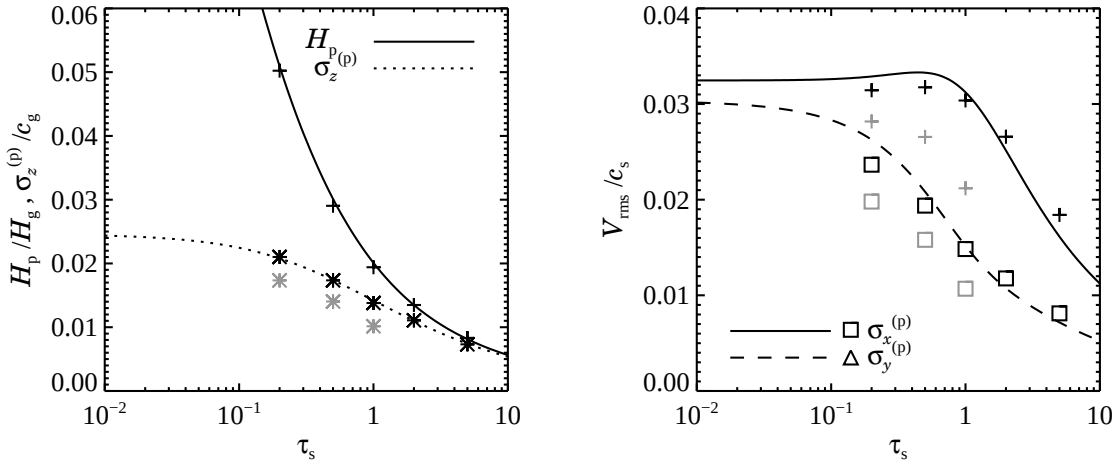

Figure 12: Comparison of simulated particle rms speeds and scale-heights to a simple analytic model of turbulent forcing that includes orbital dynamics, but no feedback[62]. Symbols are the measured rms particle speeds from single particle size simulations $\tau_{\rm s} = \Omega_{\rm K}\tau_{\rm f} = 0.2, 0.5, 1.0, 2.0, 5.0$ (128^3 grid points and 1,000,000 particles) either without (*black symbols*) or with (*grey symbols*) particle feedback. *Left plot:* Particle scale-height (*crosses*) and vertical rms speeds (*asterisks*) compared to analytical curves which use the measured vertical rms gas speed, $u_z = 0.024c_{\rm s}$ and an eddy time, $t_{\rm eddy} = 1.0\Omega_{\rm K}^{-1}$ as input. *Right plot:* Measured radial (*crosses*) and azimuthal (*squares*) particle rms speeds compared to analytic curves using the measured gas velocities (radial, $u_x = 0.032c_{\rm s}$; azimuthal $u_y = 0.030c_{\rm s}$; and correlated $\langle u_x u_y\rangle^{1/2} = 0.016c_{\rm s}$) and $t_{\rm eddy} = 1.0\Omega_{\rm K}^{-1}$ as input. See text for further discussion.

measuring the velocity components of each particle relative to a random other particle in its grid cell, calculating in the end the rms of each velocity component from the distribution of relative velocities. We make sure that the particle has a neighbour by excluding grid points with only 1 particle. We also exclude a neighbour particle if it is one of the 1000 chosen particles. This method is computationally much cheaper than the full tabulation of all collisions used in Fig. 8.

For all measurements presented in Tables 3 and 4 we have averaged over snapshots taken equidistantly 10 orbits apart, starting at $t = 20T_{\rm orb}$ where the sedimentary mid-plane layer has already had 10 orbits to form in balance with the turbulent diffusion.

We show in Table 3 the rms speeds of gas $\sigma^{(\rm g)}$ and particles $\sigma^{(\rm p)}$ for different values of the friction time (from 128^3 simulations with single-sized particles). The top part shows the results of simulations where drag force from particles on gas was not applied, whereas this back-reaction drag force is included in the bottom part of Table 3. The turbulent rms speed of the gas has in all cases a Mach number of around ${\rm Ma} = u_{\rm t}/c_{\rm s} = 0.05$ for 128^3 grid points (seen by adding up the three components quadratically), while ${\rm Ma} = 0.07$ for 64^3 grid points. The smallest particles ($\Omega_{\rm K}\tau_{\rm f} = 0.2$) have comparable rms speeds, but the rms speeds fall with stopping time as expected (see Fig. 12 and explanation below).

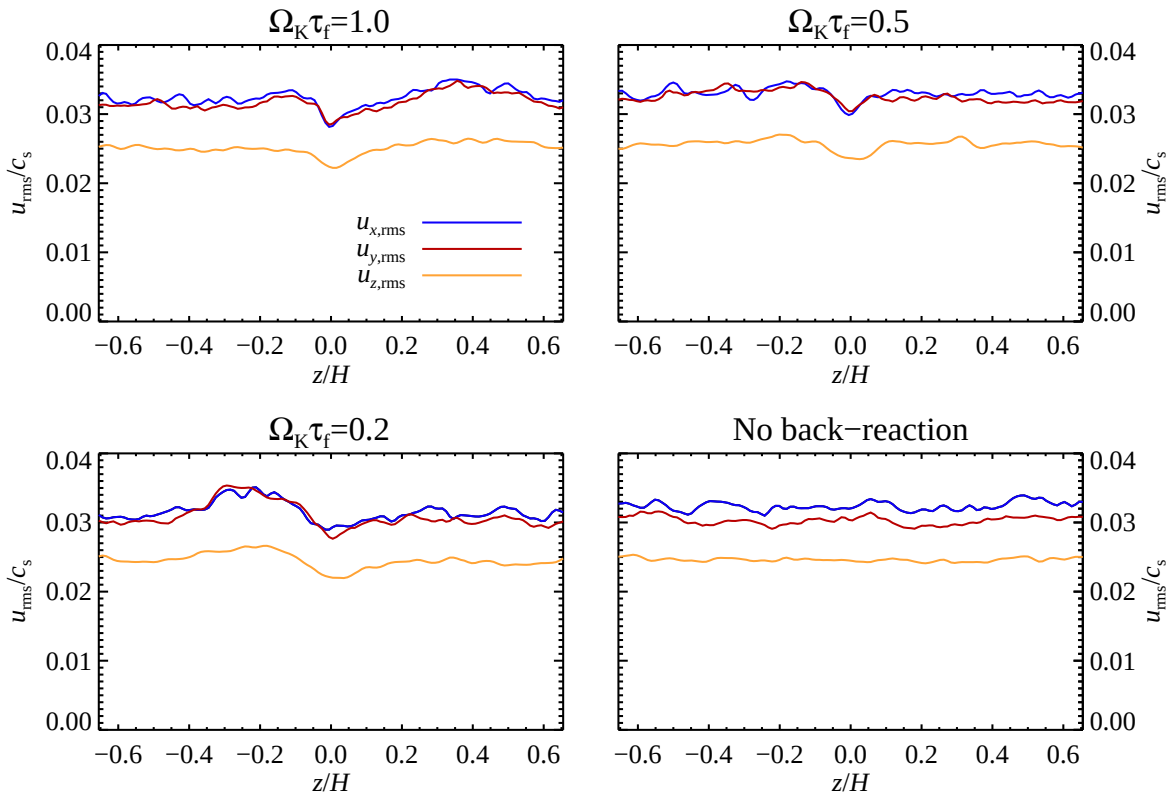

Figure 13: Gas rms speed as a function of height over the mid-plane in simulations with 128^3 grid points and 1,000,000 particles. At each z-value we have calculated the dispersion of the three velocity components. There is a clear dip in the gas velocity dispersion around the mid-plane where the solids-to-gas ratio is high. This dip is not present in the run with no back-reaction friction force (lower right panel).

To understand the simulated rms speeds of particles in MRI turbulence, we compare to Youdin & Lithwick (hereafter YL)[62]. YL consider the rms response of particles to stochastic turbulent forcing (with a temporal Kolmogorov spectrum) with orbital dynamics – in particular epicyclic motions – included, which previous works have ignored . The inputs for the simple analytic theory include the measured rms speeds of the turbulence (radial, azimuthal, vertical and the radial-azimuthal correlations), the friction time of the particles, and the eddy time, i.e. the correlation time of turbulent velocity fluctuations. Since the eddy time is a measured quantity, we treat it as a free parameter and find the reasonable value $t_{\rm eddy} \approx \Omega_{\rm K}^{-1}$.

The left panel of Fig. 12 shows that vertical speeds and scale heights of particles agree very well with the analytic theory of YL. Since vertical particle motions are decoupled from in-plane motions, the analytic description is fairly simple. When feedback is included (*grey symbols*) the random particle velocities drop, by around 25% for $\tau_{\rm s} = 1.0$ particles. This is not due to a decrease in the total turbulent Mach number (which actually goes up slightly), but likely comes from the increased particle inertia in dense clumps.

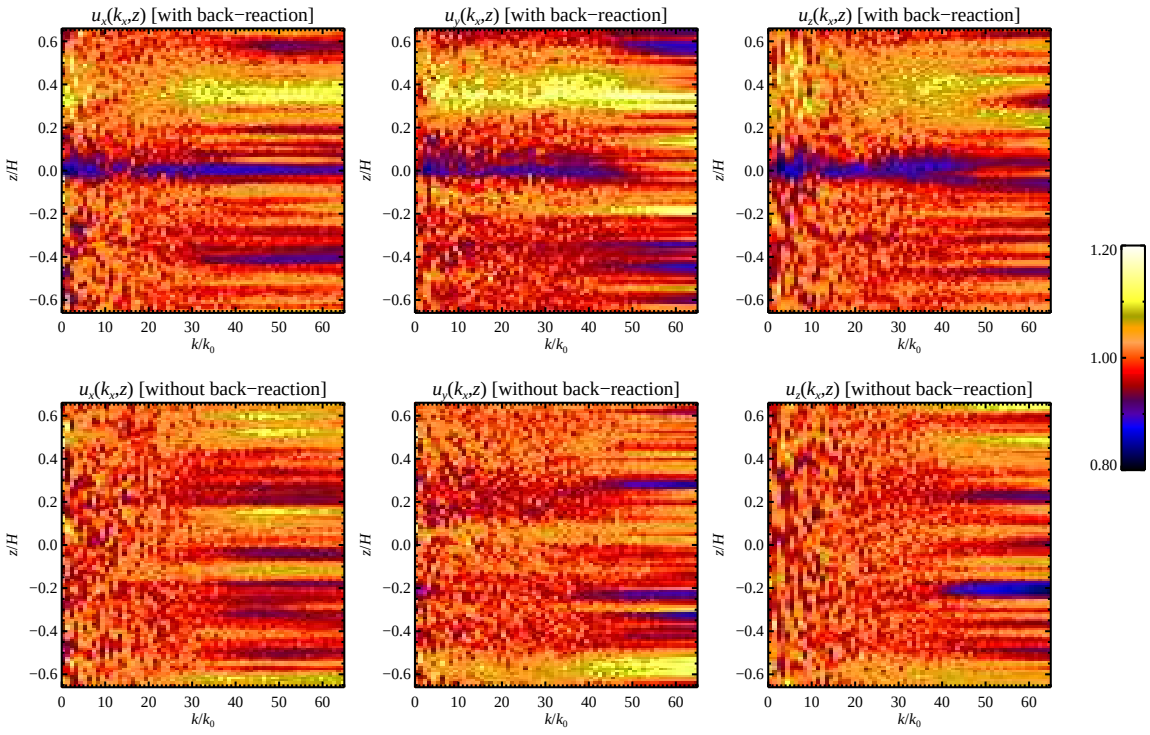

Figure 14: Normalised Fourier amplitude of the gas velocity as a function of wavenumber k (in units if the largest scale in the box k_0) and height over the mid-plane z. Shown here is a simulation with single-sized $\Omega_{\rm K}\tau_{\rm f} = 1$ particles (no self-gravity or collisional cooling). We have done 1-D Fourier transforms along the x-direction and averaged this over all values of azimuthal coordinate y and time t for each given height z. The power spectrum has been normalised with the average value at each wavenumber k. The colours represent values of $\pm 20\%$. Feedback drag force from particles on the gas reduces the velocity amplitude in the mid-plane by around 20%, explaining a similar reduction in rms speeds visible in Table 3.

The right panel of Fig. 12 shows in-plane particle velocities compared to the YL model. The agreement is good, if not as perfect as the vertical case, due to more complex dynamics. Notably, the prediction that azimuthal velocities fall before radial speeds (as $\tau_{\rm s}$ increases) due to epicyclic motion is confirmed. Drag feedback (*grey symbols*) again produces a decrease in rms speeds, by about 30% in the radial speeds for $\tau_{\rm s} = 1.0$.

It may be surprising that the eddy time-scale is so short, $t_{\rm eddy} \approx 1\Omega_{\rm K}^{-1}$ (a similar result for the eddy time was found recently by Johansen, Klahr, & Mee[63] by considering the relation between turbulent diffusion and gas rms speeds). Simple mixing length estimates based on Fig. 3 yield an eddy time at least an order of magnitude higher than our best fit value, i.e. $t_k = 1/(ku_k) \sim 100\Omega_{\rm K}^{-1}$ on the largest scales. But the large scales of the flow are dominated by Coriolis force and centrifugal terms rather than non-linear advection, and thus the correlation time of these important structures is forced to be similar to the Keplerian frequency[64,18]. Mixing length theory gives a good estimate of the life times of large scale structures, but their correlation time, which is the important quantity for mixing purposes,

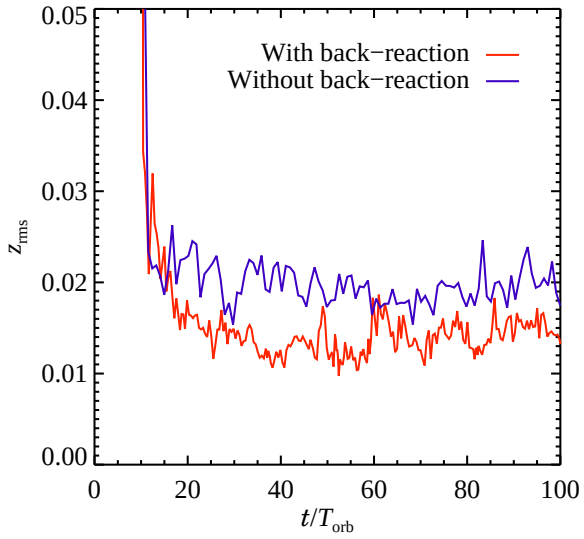

Figure 15: The root-mean-square of the particle z-coordinate as a function of time, with and without feedback, for a 128^3 simulation with single-sized $\Omega_{\rm K}\tau_{\rm f} = 1$ particles. The scale height of the particles falls by around 20% when feedback is applied, in accordance with Fig. 14 that shows that feedback damps MRI turbulence by around 20% in the sedimented mid-plane layer (the reduction in scale height is also seen in the left panel of Fig. 12).

is never longer than a Keplerian shear time $\Omega_{\rm K}^{-1}$.

The net effect of decoupling and feedback gives a total (radial, azimuthal and vertical) rms speed of $0.027c_{\rm s}$ for $\tau_{\rm s} = 1.0$, nearly half the gas rms speed of $v_t = 0.05c_{\rm s}$. Regions of high particle density damp out the gas velocity on the time-scale $\tau_{\rm g} = \tau_{\rm f}/(1+\epsilon)$ where $\tau_{\rm f}$ is the friction time of the particles and ϵ is the solids-to-gas ratio. It was shown by Dobrovolskis et al.[41] that this damping can lead to a minor reduction of turbulence around the mid-plane layer. We show in Fig. 13 the gas velocity dispersion as a function of height over the mid-plane. There is a clear, though rather modest, dip around the mid-plane where the solids-to-gas ratio is also high. The dip is only visible in simulations that include the back-reaction friction force. In Fig. 14 we show the magnitude of the different Fourier components of the gas velocity as a function of height over the mid-plane. Here we have Fourier-transformed along the x-direction and averaged over every single y coordinate at each height z. The spectrum has afterwards been normalised with the average spectrum so that differences appear more clearly. There is again a clear dip, of around 20%, in the strength of the velocity fluctuations around the mid-plane. The dip occurs at all scales, although the small scales of u_y are less affected than the large scales. In Fig. 15 we show the particle rms z-coordinate as a function of time. With particle feedback on the gas there is a drop by around 20% in the scale height of the particles, in agreement with what is expected for a $1 - 0.2^2 = 36\%$ drop in the diffusion coefficient[65].

Without feedback (128^3):

$\Omega_{\rm K}\tau_{\rm f}$	$\sigma_x^{(\rm p)}$	$\sigma_y^{(\rm p)}$	$\sigma_z^{(\rm p)}$	δv_x	δv_y	δv_z	$\delta v_x/\sigma_x^{(\rm p)}$	$\delta v_y/\sigma_y^{(\rm p)}$	$\delta v_z/\sigma_z^{(\rm p)}$
0.20	0.0307	0.0230	0.0205	0.0077	0.0078	0.0050	0.2503	0.3363	0.2432
0.50	0.0313	0.0191	0.0172	0.0126	0.0076	0.0065	0.4020	0.3942	0.3767
1.00	0.0305	0.0149	0.0138	0.0154	0.0068	0.0076	0.5018	0.4557	0.5491
2.00	0.0271	0.0120	0.0113	0.0170	0.0073	0.0092	0.6225	0.6101	0.8098
5.00	0.0186	0.0082	0.0074	0.0143	0.0062	0.0073	0.7634	0.7549	0.9836

Without feedback (64^3):

$\Omega_{\rm K}\tau_{\rm f}$	$\sigma_x^{(\rm p)}$	$\sigma_y^{(\rm p)}$	$\sigma_z^{(\rm p)}$	δv_x	δv_y	δv_z	$\delta v_x/\sigma_x^{(\rm p)}$	$\delta v_y/\sigma_y^{(\rm p)}$	$\delta v_z/\sigma_z^{(\rm p)}$
0.20	0.0428	0.0322	0.0289	0.0105	0.0093	0.0074	0.2461	0.2907	0.2588
0.50	0.0429	0.0263	0.0248	0.0147	0.0079	0.0085	0.3432	0.3013	0.3462
1.00	0.0404	0.0207	0.0198	0.0183	0.0078	0.0096	0.4533	0.3814	0.4879
2.00	0.0340	0.0161	0.0152	0.0191	0.0082	0.0109	0.5572	0.5099	0.7199
5.00	0.0237	0.0115	0.0104	0.0170	0.0078	0.0094	0.7163	0.6847	0.9072

With feedback (128^3):

$\Omega_{\rm K}\tau_{\rm f}$	$\sigma_x^{(\rm p)}$	$\sigma_y^{(\rm p)}$	$\sigma_z^{(\rm p)}$	δv_x	δv_y	δv_z	$\delta v_x/\sigma_x^{(\rm p)}$	$\delta v_y/\sigma_y^{(\rm p)}$	$\delta v_z/\sigma_z^{(\rm p)}$
0.20	0.0276	0.0194	0.0172	0.0068	0.0065	0.0044	0.2463	0.3376	0.2555
0.50	0.0279	0.0166	0.0150	0.0108	0.0065	0.0054	0.3845	0.3855	0.3569
1.00	0.0220	0.0111	0.0106	0.0109	0.0049	0.0055	0.4982	0.4501	0.5224

With feedback (64^3):

$\Omega_{\rm K}\tau_{\rm f}$	$\sigma_x^{(\rm p)}$	$\sigma_y^{(\rm p)}$	$\sigma_z^{(\rm p)}$	δv_x	δv_y	δv_z	$\delta v_x/\sigma_x^{(\rm p)}$	$\delta v_y/\sigma_y^{(\rm p)}$	$\delta v_z/\sigma_z^{(\rm p)}$
0.20	0.0423	0.0291	0.0265	0.0108	0.0094	0.0072	0.2579	0.3224	0.2715
0.50	0.0372	0.0224	0.0217	0.0144	0.0082	0.0073	0.3892	0.3622	0.3364
1.00	0.0388	0.0182	0.0184	0.0187	0.0082	0.0088	0.4855	0.4361	0.4798

Table 4: Particle rms speeds ($\sigma^{(\rm p)}_{x|y|z}$), collision speeds ($\delta v_{x|y|z}$) and their ratios. The top part of the table shows results without drag force on the gas, the bottom part includes drag force on the gas. The collision speeds are very low for small particles, but the ratio between collision speed and rms speed increases with increasing friction time as the equal-sized marginally coupled particles are big enough to have significantly different histories when they meet. Back-reaction friction force on the gas has very little influence on the ratio of collision speeds to rms speeds. There is a 10-20% increase in the ratio of collision to rms speed when going from 64^3 to 128^3 grid points, possibly due an expansion of the inertial range of the turbulence. Higher resolution studies will be needed to determine whether this trend continues of whether the collision speeds have already converged.

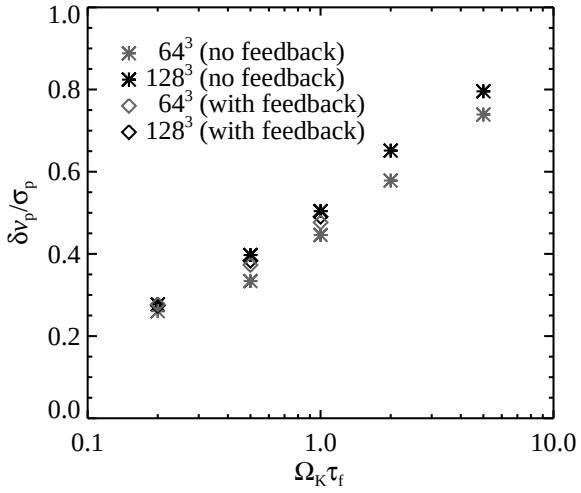

Figure 16: The ratio of particle collision speed $\delta v_{\rm p}$ to large scale particle rms speed $\sigma_{\rm p}$, both calculated as quadratic sums of the directional components given in Table 4 and shown for two resolutions and with and without particle feedback on the gas. The collision speeds increase as expected with increasing friction time as particles decouple from fast large scale eddies. Collision speeds increase by 10-20% when increasing resolution from 64^3 to 128^3, likely because the inertial range of the gas turbulence expands to smaller scales. Feedback has only little influence on the ratio of collision speed to rms speed, but the overall rms speed of particles is reduced by feedback (see Fig. 12). Higher resolution studies will be needed to determine whether $\Omega_{\rm K}\tau_{\rm f}=1$ particles will eventually obtain the fully mixed $\delta v_{\rm p}/\sigma_{\rm p}=\sqrt{2}$.

1.11.2 Why are collision speeds so low?

Table 4 shows the collision speed δv of the particles for comparison with the particle rms speeds. Here we have chosen a thousand particles throughout the simulation and calculated their relative speed with a random different particle in the same grid cell. The collision speed of marginally coupled particles (with $\Omega_{\rm K}\tau_{\rm f}=1$) is around 50% of the overall rms speed. This factor 2 decrease in the relative speeds on small scales compared to rms speeds remains to be explained. An exact analytic prediction of this effect is difficult, and has not to our knowledge been done with either orbital dynamics or feedback, let alone both effects. Higher resolution simulations will be needed to determine if small scale eddies can change this result. Fig. 3 indicates that over an order of magnitude in the inertial range is resolved, but scales around the onset of the dissipative subrange may be important for collision speeds.

We can think of two possible reasons for the low collision speeds. The first is insufficient numerical resolution. The numerical dissipation of the code results in an underestimate of the amplitude of turbulent velocities at scales smaller than around 6 grid points. At the same scales, the particle-mesh drag force (§1.2) begins to be underestimated[37]. Taking the stopping length of the boulders to be $\ell_{\rm stop}=\tau_{\rm f}v_{\rm rms}$, where $v_{\rm rms}$ potentially depends on $\tau_{\rm f}$, this yields for marginally coupled particles a stopping length of $\ell_{\rm stop}=0.025H$, when reduction of the rms

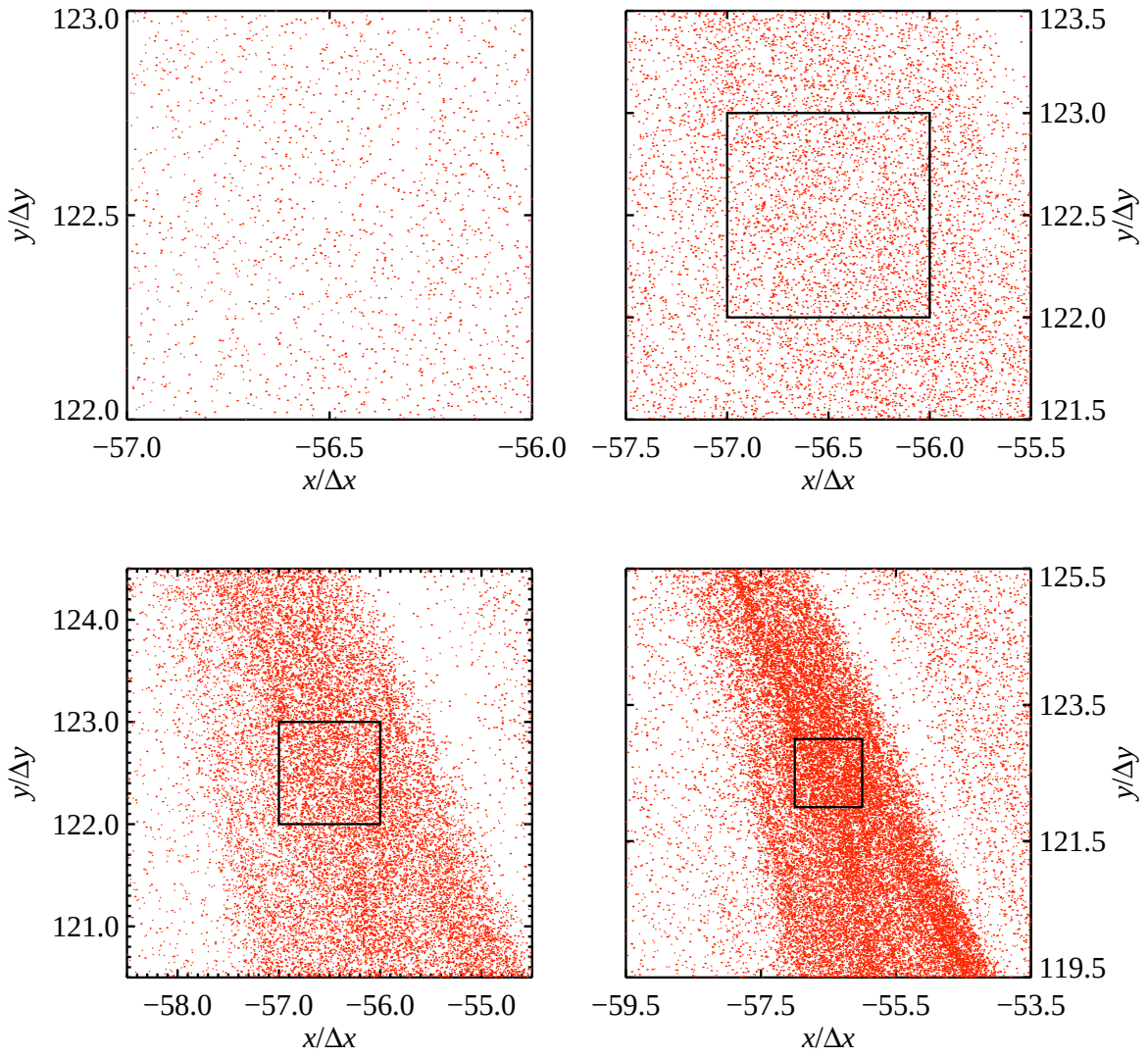

Figure 17: Particles in the densest grid cell at $t = 20T_{\rm orb}$ for the 256^3 simulation presented in the main paper (this is before collisional cooling and self-gravity are turned on). The panels show a gradual zoom out on the surrounding grid cells (still in the same z-plane). No spurious structure is evident either at the subgrid scale or at the interfaces between grid cells, since the high order particle-mesh drag force scheme samples 27 nearby grid points when evaluating the gas velocity at the position of a particle. The particles are shown in velocity space in the left panel of Fig. 19.

speed due to marginal coupling and feedback is taken into account. The resolution is either $\delta x = 0.01$, for 128^3 grid cells, or $\delta x = 0.005$ for 256^3 grid cells. If we assume that relative collision speed between particles of stopping length $\ell_{\rm stop}$ is typically given by turbulent eddies of wavelength $2\ell_{\rm stop}$, then these eddies are of size 5-10 grid cells, depending on resolution. Thus there is potentially a damping of the collision speeds, as some of the scales that are

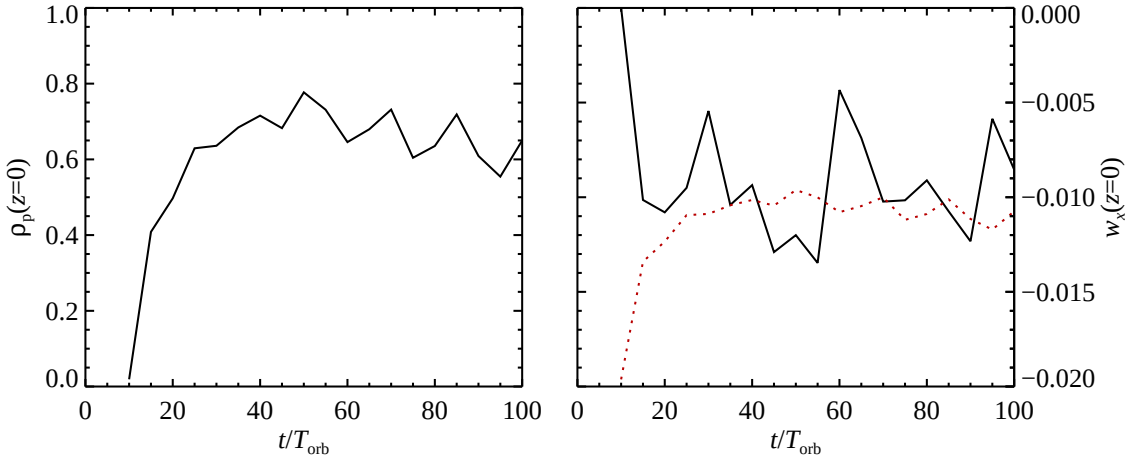

Figure 18: The mean particle density in the mid-plane (left panel) for a simulation with single-sized $\Omega_{\rm K}\tau_{\rm f} = 1$ particles and feedback on the gas. The right panel shows the radial velocity w_x of the particles in the mid-plane. Isolated particles would have $w_x = -0.02c_{\rm s}$, but the increased inertia in the mid-plane has decreased the radial drift by a factor two there. The dashed line shows the expected radial velocity calculated from the mid-plane density shown in the left plot. There is relatively good agreement, an indication that drag forces are calculated correctly in the code (we note that a thorough test of the particle-mesh drag force scheme was performed by Youdin & Johansen[37]). Radial drift is a bit lower than expected, but that may be explained by large scale gas density fluctuations that modify the radial pressure gradient enough to slow the radial drift of marginally coupled particles[9].

important for relative motion are just at the onset of the dissipative subrange. Table 4 and Fig. 16 show that the ratio of collision speeds to rms speeds does increase by 10-20% when going from 64^3 to 128^3 grid points, although the increase is much more modest when feedback is included. An increase in grid resolution, implying both an increased inertial range and a sharpening of the particle-mesh scheme at small scales, will be needed to determine whether the collision speeds will continue to go up with increasing resolution.

A second possible explanation is missing orbital dynamics in analytical estimates. The collision speeds predicted by Voelk et al.[66] rely on a Kolmogorov spectrum with eddy turn over times from mixing length theory. This approach does not take into account epicyclic motion, nor the upper limit to structure correlation times given by the Coriolis force. YL already showed that orbital dynamics are important for particle rms speeds, but there is no similar theory for collision speeds that takes into account orbital dynamics. Such analytical work should be a high priority for future research because of its importance to the dynamics and growth of boulders across the m-sized barrier.

We note that the particle-mesh drag force scheme of the Pencil Code has been extensively tested in the recent paper by Youdin & Johansen[37]. The same TSC assignment/interpolation scheme is also used for self-gravity, for which we present a test problem in §1.3.1.

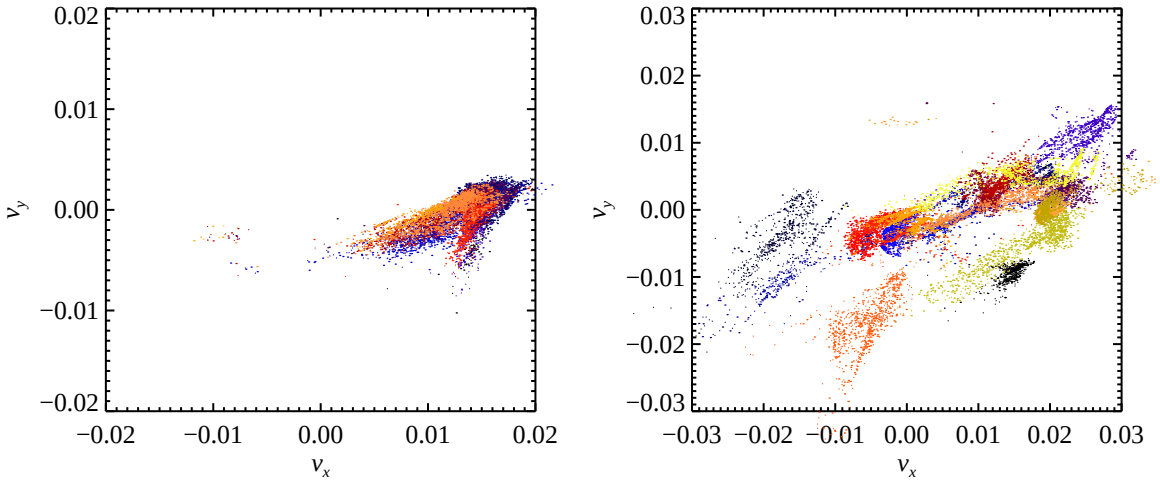

Figure 19: Particles shown in velocity space (v_x, v_y). The left panel shows the particles from Fig. 17 – the colours refer to the 16 individual grid points in the lower right panel of Fig. 17. The right panel shows a 128^3 simulation with single-sized $\Omega_{\rm K}\tau_{\rm f} = 1$ particles. Notice the higher axis range. Here we have chosen 20 random grid points containing between 500 and 1000 particles. The overall spread of particle velocities is large, comparable to $0.02c_{\rm s}$ in each direction, whereas the spread within individual grid cells is much smaller. The positive correlation between the two velocity components arises from the positive Reynolds stress of the MRI turbulence.

We proceed with a few reality checks of particle positions in physical space and in velocity space. While we do not claim that any of these tests are exhaustive, they are meant to serve the purpose to exclude that spurious particle structure at the grid scale is the source of the low collision speeds. We show in Fig. 17 particle positions around the densest grid point at $t = 20T_{\rm orb}$ for the 256^3 simulation presented in the main paper, before collisional cooling and self-gravity are turned on. No spurious structure is evident at subgrid scales or at the interfaces between the grid cells. In Fig. 18 we show the mean particle density in the mid-plane as a function of time (left panel), for a simulation with single-sized $\Omega_{\rm K}\tau_{\rm f} = 1$ particles. The right panel of Fig. 18 shows the mean radial drift velocity in the mid-plane. Particles drift slower than the expected $-0.02c_{\rm s}$ due to increased particle inertia in the mid-plane[39]. The dashed line indicates the expected drift velocity given the mid-plane density shown in the left panel. It is in relatively good agreement with the measured drift, another indication that the code applies drag forces correctly. A slight decrease in the drift speed may be due to large scale pressure gradients in the gas slowing down the radial drift[9].

Finally we show in Fig. 19 particle positions in velocity space (v_x, v_y). While the overall spread in velocities is large, the individual grid cells (shown with individual colours) show a much more coherent velocity structure. We hope to explain this difference in future publications, both with increased numerical resolution and with improved analytical models that include orbital dynamics on the calculation of the collision speeds.

1.12 Low ionisation discs

A high enough ionisation fraction is needed for the magnetorotational instability to operate[67]. This threshold may be reached in hot parts of the disc and in parts where the column density is low enough that cosmic rays penetrate[68,69,70]. Typically a penetration depth of $\Sigma_{\rm g} \approx 100\,{\rm g\,cm^{-2}}$ is found. Other sources of ionisation are decay of radioactive elements and chemical reactions. Small dust grains, on the other hand, soak up electrons and reduce the conductivity[71]. This has lead to the concept of a dead zone in the midplane of the disc where ionisation is insufficient for MRI[21]. Several mechanisms have been proposed for reviving the dead zone: growth of the peak dust grain size by an order of magnitude[71], using the turbulent kinetic energy to ionise molecules, thus maintaining any turbulence that is already present[72], and X-ray flares from the central star that would ionise the disc periodically[73].

We investigate the limit in which the MRI completely fails to influence the midplane by modelling the same problem as in the main text, but absent magnetic fields. A more advanced model would still have magnetically active surface layers that could influence the "dead zone" dynamically[74,75,76]. We do not, in general, expect density fluctuations in the gas similar to what happens in the MRI. This is because the Mach number of Kelvin-Helmholtz turbulence and streaming turbulence is generally smaller than for the MRI[11,12]. This situation may change in a more advanced model with active surface layers that can influence the magnetically dead mid-plane, as the surface layers send density waves through the dead zone[74,76].

1.12.1 Low radial pressure support

We show in Fig. 20 the evolution of the sedimented mid-plane layer for the usual range of particle sizes and a radial pressure support of $\Delta v = -0.02 c_{\rm s}$. The box size was set to $L_x = L_y = L_z = 0.1H$, 1.32 times smaller than in the magnetic runs, in order to resolve the thin mid-plane layer that forms in the absence of global MRI turbulence. A turbulent state develops anyway since vertical shear in the radial and azimuthal gas flow is unstable to the Kelvin-Helmholtz instability[5,77,7,13,78,11]. The streaming instability is also a source of non-linear dynamics and turbulence[10,37,12].

It is evident from Fig. 20 that the particles quickly gather at a single radial location and drift radially together for the full duration of the simulation (50 orbits, the Courant time-step in these small boxes limits the possible simulation times compared to the magnetic runs). This can be understood as an effect of the streaming instability. Any isolated particle drifts quickly into the overdense band where the dynamics is so dominated by particles that the radial drift is significantly reduced. Very high particle densities are reached within the band, with peaks at more than three orders of magnitude times the gas density.

The high particle densities are very susceptible to gravitational collapse. We show in Table 5 that gravitational collapse is possible in discs with as low mass as one half of the MMSN. The accretion rate of the most massive bound cluster is generally 3 orders of magnitude lower than in the magnetic runs, which follows the expected trend of equation (46) that the mass of the bound object scales with the cube of the column density. The solid size of the most massive bound cluster in the 128^3 run of Table 5 is 150 km, smaller than in the runs with

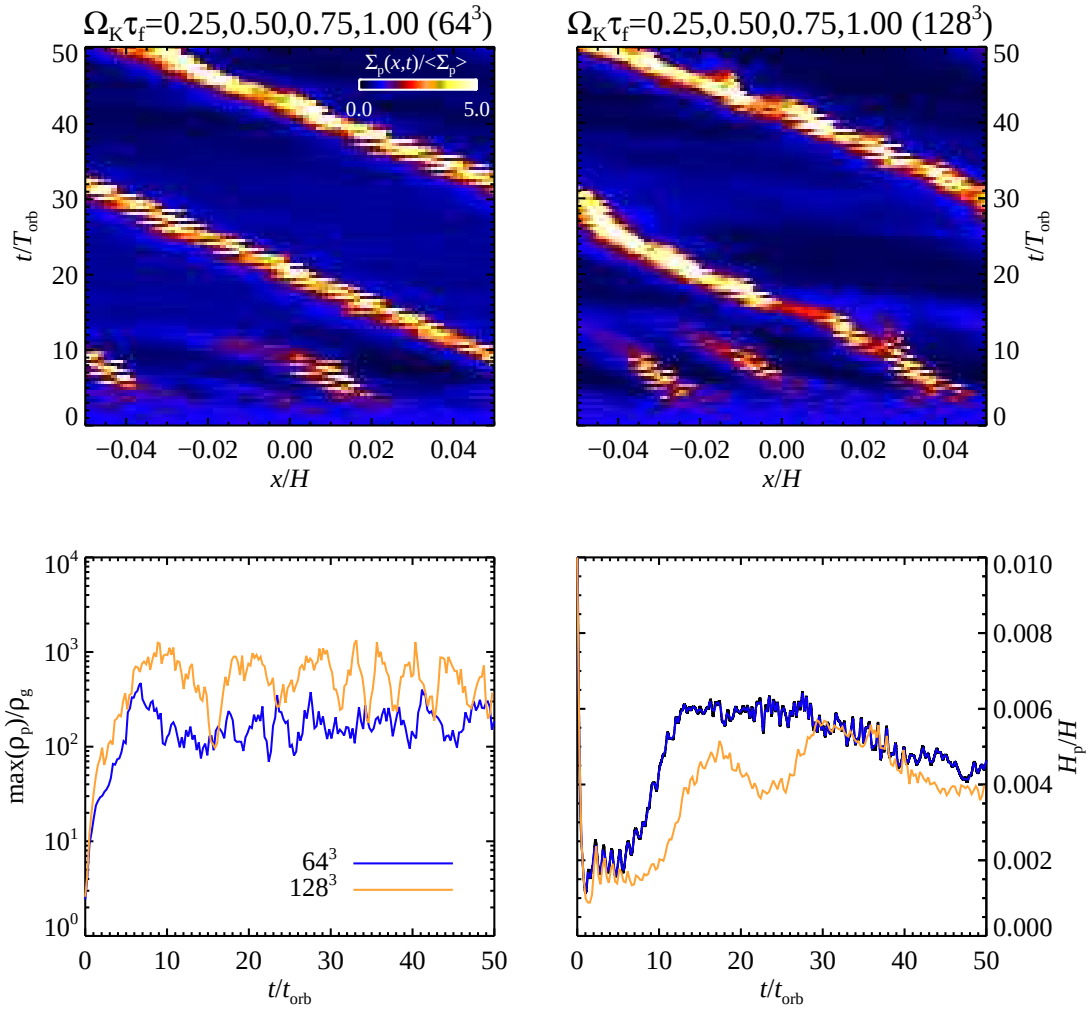

Figure 20: Particle column density for 64^3 and 128^3 simulation with no magnetic fields and the usual range of boulder sizes. Particles quickly end up in a single azimuthally extended roll and slowly drift in together for at least 50 orbits. The maximum bulk density of particles reaches 1000 times the ambient gas density.

magnetorotational turbulence presented in the main text, but still larger than the classical view of planetesimals.

1.12.2 Moderate radial pressure support

We show in Fig. 21 a comparison between two 3-D simulations: one with magnetic fields and one without. Both have a resolution of 128^3 grid points, marginally coupled particles with $\Omega_K\tau_f = 1$ and a moderate radial pressure support of $\Delta v = -0.05c_s$. The box size is $L_x = L_y = L_z = 1.32H$ for the MRI run and $L_x = L_y = L_z = 0.2H$ for the run with no magnetic fields. After an initial period where strong density enhancements form, the solids-

Resolution	$N_{\rm par}/10^6$	$\Delta t_{\rm grav}$	$\tilde{G}$	Q	$N_{\rm clusters}$	$\dot{M}_{\rm cluster}$
(1)	(2)	(3)	(4)	(5)	(6)	(7)
64^3	0.125	5.0	0.1	16.0	1	0.0050
128^3	1.0	5.0	0.025	64.0	2	0.0007

Table 5: Resolution study for runs with no magnetic fields and $\Delta v = -0.02 c_{\rm s}$. Col. (1): Mesh resolution. Col. (2): Number of superparticles in millions. Col. (3): Number of orbits with self-gravity. Col. (4): Minimum self-gravity parameter where gravitationally bound clusters form (MMSN has $\tilde{G} \approx 0.05$ at $r = 5$ AU). Col. (5): Corresponding Toomre $Q \approx 1.6 \tilde{G}^{-1}$. Col. (6): Number of clusters at the end of the simulation. Col. (7): Accretion rate of the most massive cluster in Ceres masses per orbit.

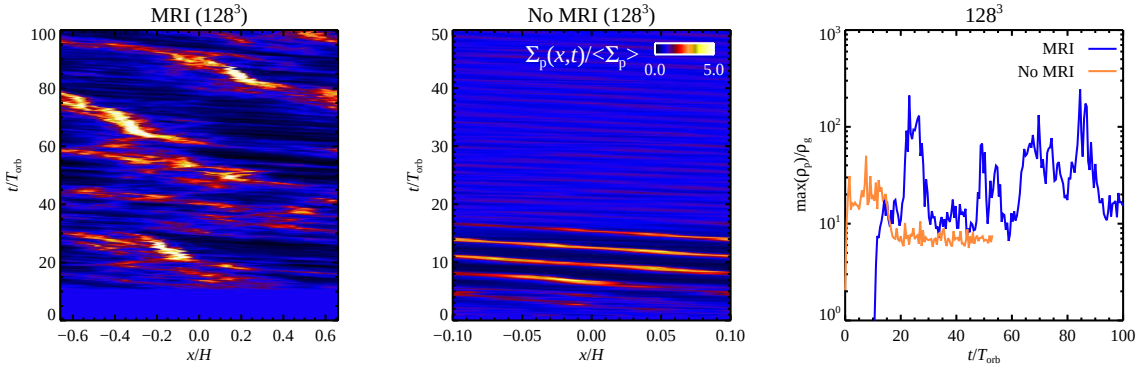

Figure 21: Comparison of azimuthally averaged boulder column density for models with magnetic fields (left plot) and without magnetic fields (middle plot) for 128^3 grid points and marginally coupled particles with $\Omega_{\rm K}\tau_{\rm f} = 1$. The model with no magnetic fields initially shows some clumping and overdensities, but these die out after 20 orbits after which the maximum solids-to-gas ratio stays below 10 for the duration of the simulation with no signs of the high density events that are obvious in the MRI run.

to-gas ratio never rises above 10 in the simulation without magnetic fields. In Fig. 22 we show the time evolution of particle density averaged over the azimuthal direction for the moderate pressure support non-magnetic run presented in the middle panel of Fig. 21. The particle density reaches a configuration where a single standing wave dominates the box, with no significant overdensities. This state may come about because of the streaming instability. It was observed by Johansen & Youdin[12] that marginal coupling produces a very strongly turbulent state (with vertical diffusion coefficients similar to those of the MRI). This state was nevertheless very clumpy in the simulations of Johansen & Youdin[12], but the inclusion of vertical gravity in the current work may mean that the correlation times are so short (due to vertical oscillations) that clumping is suppressed. The simulations by Johansen & Youdin[12] also showed that a higher background solids-to-gas ratio leads to a dramatic increase in growth rate of the streaming instability, and a decrease in the unstable wavelengths. We show in the next section (§1.12.3) that a slight increase in the global solids-to-gas ratio indeed leads to significant particle clumping.

Resolution	$N_{\rm par}/10^6$	$\Delta t_{\rm grav}$	$\tilde{G}$	Q	$N_{\rm clusters}$	$\dot{M}_{\rm cluster}$
(1)	(2)	(3)	(4)	(5)	(6)	(7)
64^3	0.125	5.0	0.05	32.0	1	0.092
128^3	1.0	5.0	0.025	64.0	3	0.004

Table 6: Resolution study for runs with no magnetic fields, $\Delta v = -0.05 c_{\rm s}$ and $\epsilon_0 = 0.03$. Col. (1): Mesh resolution. Col. (2): Number of superparticles in millions. Col. (3): Number of orbits with self-gravity. Col. (4): Minimum self-gravity parameter where gravitationally bound clusters form (MMSN has $\tilde{G} \approx 0.05$ at $r = 5$ AU). Col. (5): Corresponding Toomre $Q \approx 1.6\tilde{G}^{-1}$. Col. (6): Number of clusters at the end of the simulation. Col. (7): Accretion rate of the most massive cluster in Ceres masses per orbit.

We have tested the effect of self-gravity in the 3-D non-magnetic models with moderate radial pressure support as well, with the four different particle sizes we used in the models described in the main letter. We have not been able to form accreting self-gravitating clusters, like those we observe in discs with MRI turbulence, for any reasonable column density $\tilde{G} < 1$ at either 64^3 or 128^3 resolution. Global magnetorotational turbulence thus appears to overall promote rather than impede gravitational collapse of marginally coupled boulders.

1.12.3 Higher solids-to-gas ratio

We performed simulations with increasingly higher solids-to-gas ratio with the expectancy that the turbulent state would get weaker and overdensities larger. This behaviour was indeed confirmed. In Fig. 23 we show the evolution of the mid-plane layer for moderate radial pressure support and a background solids-to-gas ratio of 0.03. Extremely high overdensities, up to three orders of magnitude higher than the gas, now occur. We show in Table 6 the gravitational collapse for the moderate pressure support case. The accretion rate is around six times higher than in the case of low radial pressure support (see Table 5), but that is probably due to the increased global solids-to-gas ratio in the moderate pressure support case.

One possible way to enhance the global solids-to-gas ratio is by radial drift augmentation[49,6,50]. This would be especially likely in the case of a magnetically active and warm outer disc with a strong radial drift. Drifting into the dead inner regions of the disc the boulder velocity field would converge at the rim of the dead zone, leading to particle pileups there. Another effect, which to our knowledge has not yet been explored, is that the accreting surface layers must lose all their solids to the dead zone. Considering an active layer with a width of one gas scale height H and an orbital distance r, the probability for a small dust grains to accrete all the way to the star without diffusing into the dead zone is only $(H/r)^2 \ll 1$. Once a grain is lost into the dead zone it is very unlikely that it will diffuse back into the active layers because the turbulent diffusion in the dead zone is assumed to be very low. A third possibility for augmenting the solids-to-gas ratio is by photoevaporation of the gaseous part of the disc[29]

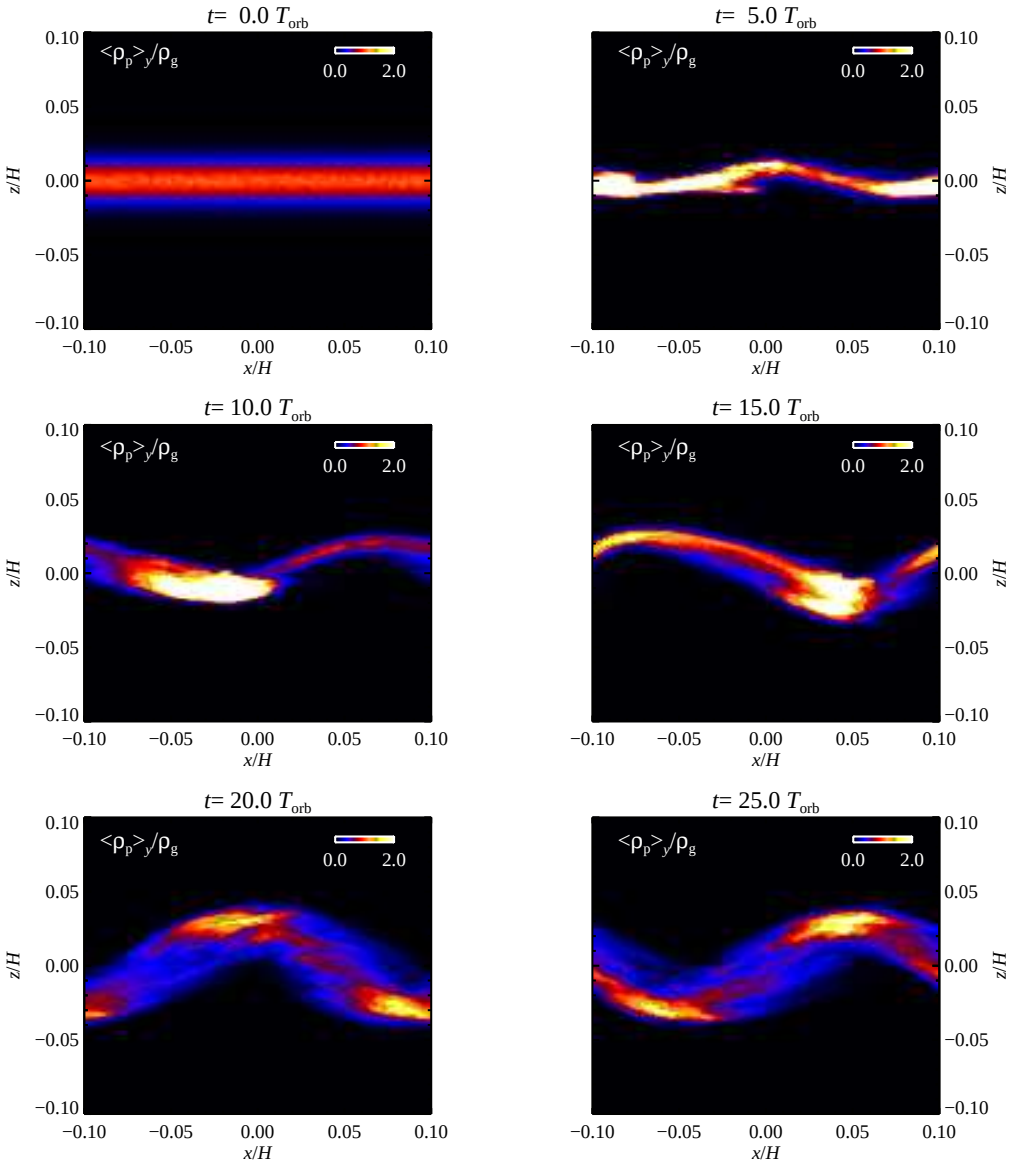

Figure 22: Time evolution of the boulder density averaged over the azimuthal y-direction in a 3-D simulation with 128^3 grid points and 10^6 marginally coupled particles with $\Omega_{\rm K}\tau_{\rm f} = 1$. A Kelvin-Helmholtz instability develops from the initial sedimentation, driven by the shear in the radial drift velocity of the gas[39]. The whole particle layer eventually participates in a single standing wave where particles drift and oscillate around the midplane (see main text for details).

1.13 Heating and cooling

Drag and collisions dissipate the kinetic energy of the solids. In the extreme case, all this heat is released locally in the gas. We consider here the case of ineffective radiative cooling

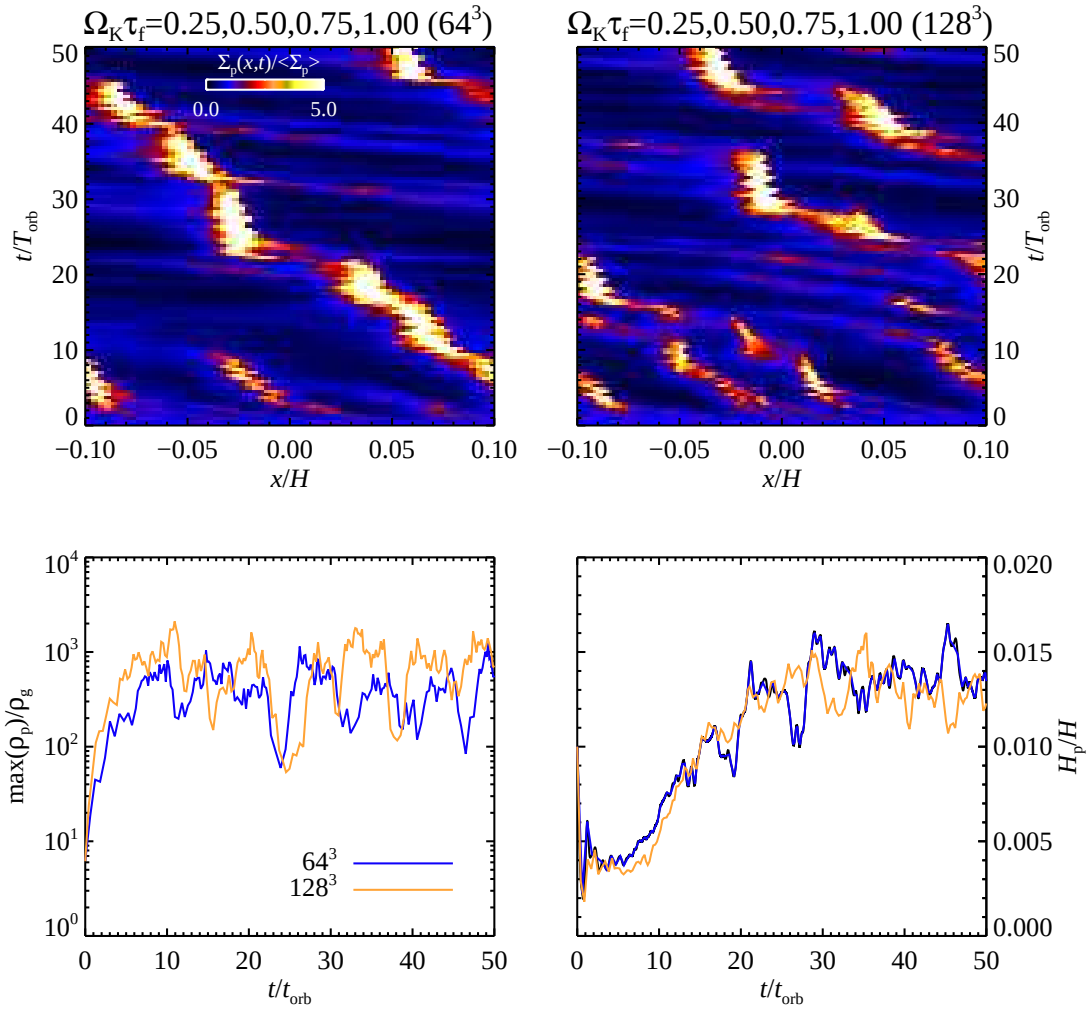

Figure 23: Particle column density for a global solids-to-gas ration of 0.03. The particle density peaks at more than three orders of magnitude higher than the gas density.

and an ideal gas equation of state, rather than the isothermal equation of state assumed in the rest of the paper. The only means to transport energy in this model is by turbulent heat conduction. In reality collisional cooling may transfer most of the energy into deformation of the colliding bodies, but we consider here the effect of the most extreme case of local heating on gravitational collapse.

We have ignored viscous heating under the assumption that the gas background has found an equilibrium between radiative loses and viscous heating. The extra gas shear and compression in the collapsing particle clusters is negligible due to the pressure support of the gas, so any extra viscous heating in regions of collapse is not important. We have found no traces of the gravitationally contracting clusters in the gas density or in the gas velocity field (gas is allowed to exert and feel self-gravity in the simulations that include heating).

We show in Fig. 24 the gas temperature as a function of time for a run with 64^3 grid points

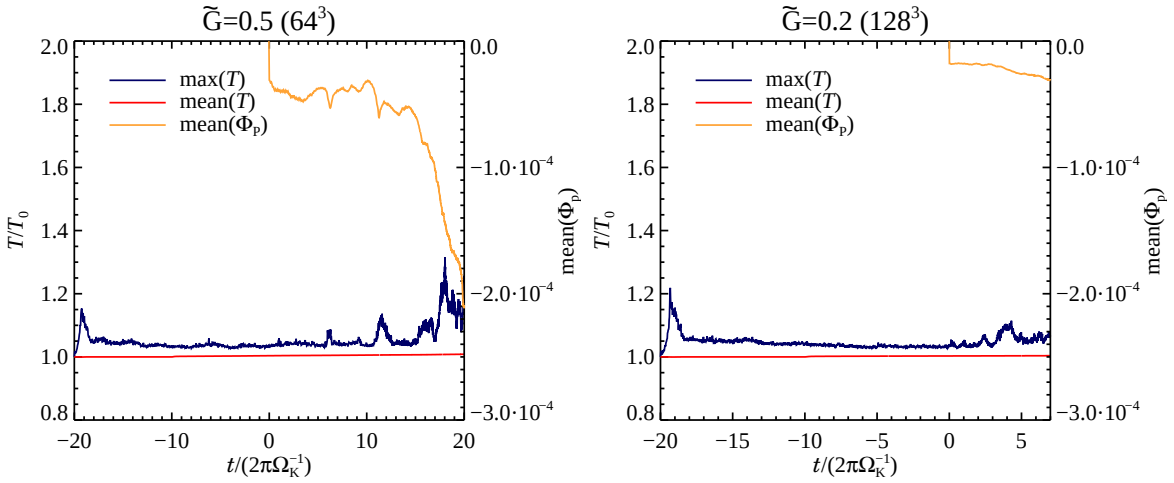

Figure 24: The maximum and mean temperature of the gas as a function of time in our adiabatic model, for models with 64^3 zones and $\tilde{G} = 0.5$ (left), and 128^3 zones and $\tilde{G} = 0.2$. Self-gravity is turned on at $t = 0$; the first collapse, seen in the fall in the mean potential of the particles, begins after approximately 10 orbits for the 64^3 run. Peaks in the maximum temperature coincide well with times where gravitational energy is released (the peak at $t = -20$ is due to compression in the initial random velocity field). The energy is transferred to the gas by drag and inelastic collisions. The mean temperature rises negligibly because gravitational collapse occurs in only a small fraction of the total gas volume.

and $\tilde{G} = 0.5$ (a 25% higher column density was needed for collapse in this case, which we attribute simply to the stochastic nature of the collapse) and for a run with 128^3 and the usual $\tilde{G} = 0.2$. Self-gravity is turned on at a time $t = 0$. We let gas exert and feel self-gravity in the simulations with heating, although this causes no real difference in the behaviour. This effect is otherwise not included in the simulations (see §1.5.3). The maximum temperature rises to no more than 30% over the initial value at times of gravitational collapse (seen in the mean gravitational potential energy of the particles). Peaks in the maximum temperature coincide well with gravitational energy release events. The peak at $t = -20$ happens due to compression in the initially random velocity field.

We show in Fig. 25 the dissipation rate of drag and collisions. Drag dominates the volume-averaged energy budget, with a heating rate at least six orders of magnitude higher, because collisions are only important in the few grid points where the solids-to-gas ratio greatly exceeds unity. Assuming a temperature of around 80 K in the non-heated state, the temperature reaches a maximum of approximately 104 K in the 64^3 simulation, still too low to even melt the icy component of the boulders.

1.14 Varying radial pressure support

Cuzzi et al.[13] gives a detailed review of the values expected for the radial pressure support parameter. We have assumed throughout this work a radial pressure support of either

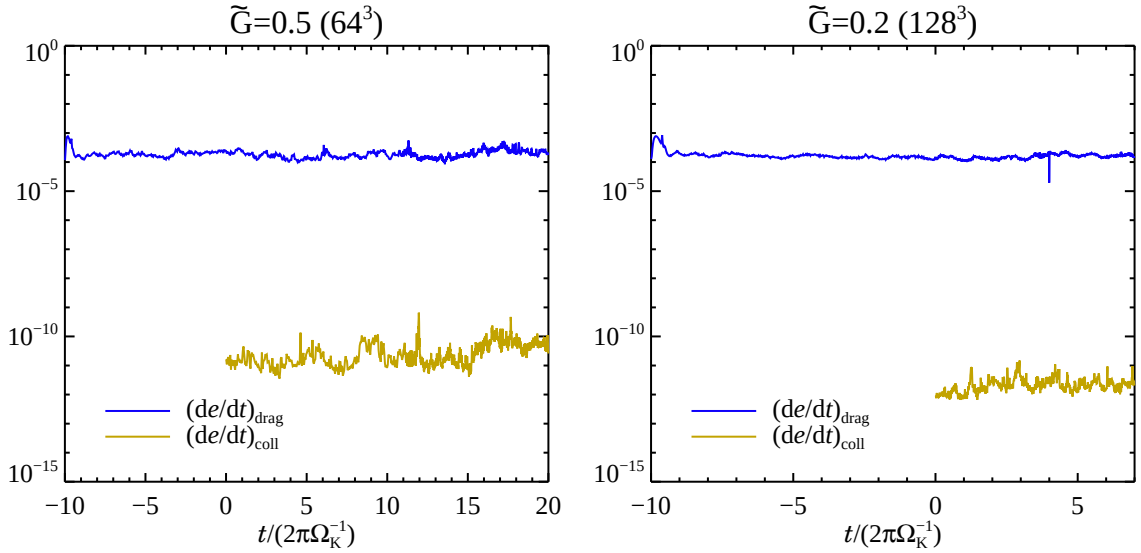

Figure 25: Volume-averaged heating rate by drag (dark/blue) and by inelastic collisions (bright/khaki) in the same runs shown in Fig. 24. Drag force dissipates six orders of magnitude more kinetic energy than collisions do, although collisional dissipation dominates in regions where the bulk density of solids is at least two orders of magnitude higher than the gas (see §1.4).

Resolution	$N_{\rm par}/10^6$	$\Delta t_{\rm grav}$	α	$\tilde{G}$	Q	$N_{\rm clusters}$	$\dot{M}_{\rm cluster}$
(1)	(2)	(3)	(4)	(5)	(6)	(7)	(8)
64^3	0.125	10.0	0.002	0.7	2.3	1	2.7
128^3	1.0	7.0	0.001	0.4	4.0	4	2.6

Table 7: Resolution study for $\Delta v = -0.05 c_{\rm s}$. Col. (1): Mesh resolution. Col. (2): Number of superparticles in millions. Col. (3): Number of orbits with self-gravity. Col. (4): Measured turbulent viscosity. Col. (5): Minimum self-gravity parameter where gravitationally bound clusters form (MMSN has $\tilde{G} \approx 0.05$ at $r = 5$ AU). Col. (6): Corresponding Toomre $Q \approx 1.6\tilde{G}^{-1}$. Col. (7): Number of clusters at the end of the simulation. Col. (8): Accretion rate of the most massive cluster in Ceres masses per orbit.

$(\partial \ln P/\partial \ln r)(H/r) = -0.04$ or $(\partial \ln P/\partial \ln r)(H/r) = -0.1$ (see §1.5.1). The value of H/r directly yields the local temperature when folded with the mass of the central object and the orbital radius in the disc. We have run test simulations of colder discs as well, with $H/r = 0.02$, corresponding to a four times lower temperature at a given location than models with $H/r = 0.04$. In Fig. 26 we compare the evolution of the maximum particle density between the standard run with $H/r = 0.04$ and the cold run with $H/r = 0.02$. The two curves are statistically indistinguishable. Lowering the disc aspect ratio reduces radial drift and decreases the unstable wavelengths of the streaming instability, but this apparently does not change the evolution of the solids, at least for moderate changes in temperature.

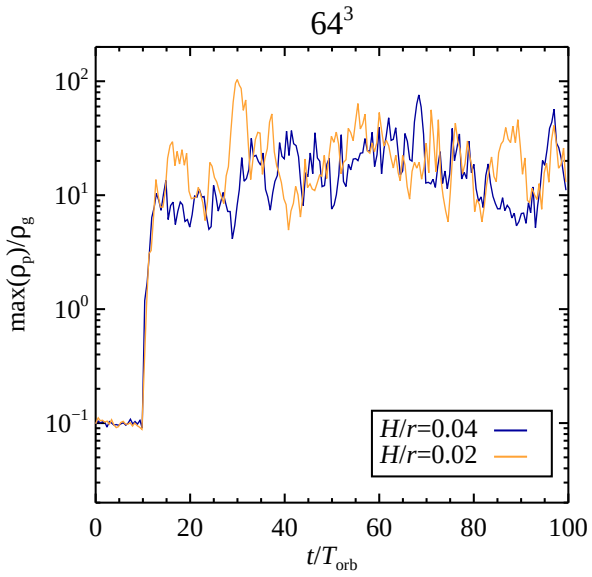

Figure 26: Maximum particle density versus time for standard run with $H/r = 0.04$ (blue) and a colder disc with $H/r = 0.02$ (yellow). The curves appear statistically indistinguishable. A lower disc aspect ratio decreases the radial drift of the solids, while making the unstable wave lengths of the streaming instability smaller, but apparently neither of these effects significantly changes the particle overdensities in the considered cases.

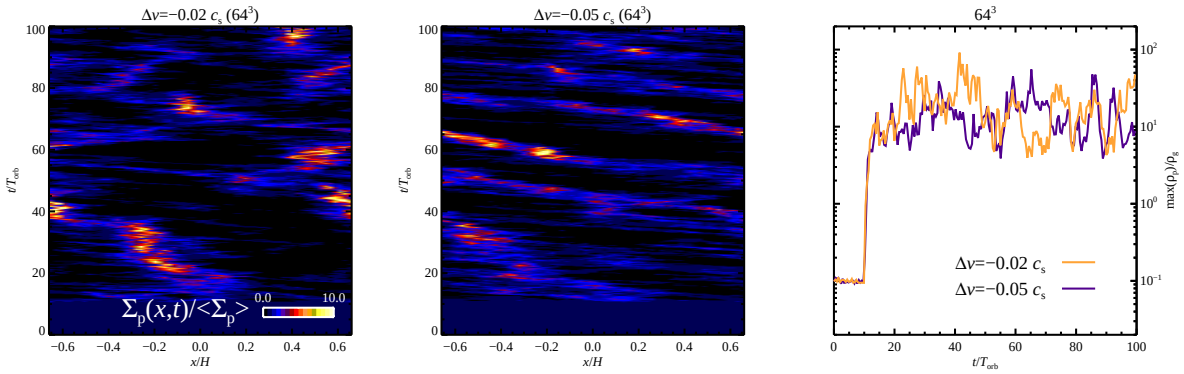

Figure 27: Comparison of the topography of the particle layer for the standard run with $\Delta v = -0.02 c_s$ (left) with a run with 2.5 times stronger radial pressure support $\Delta v = -0.05 c_s$ (middle), both at 64^3 grid points and 125,000 particles. The increased radial drift is clear in the tilted bands, but the streaming instability still produces strong overdensities in the particle layer. The right plot shows the maximum particle density as a function of time – the peaks in the particle density are reduced by around 30% in the case of the stronger radial pressure support.

A higher radial pressure support can occur for a given value of H/r if the radial pressure support $|\partial \ln P / \partial \ln r|$ exceeds unity. We next examine the consequences of a higher radial

State	$\langle\rho_\mathrm{p}\rangle/\langle\rho_\mathrm{g}\rangle$	$\tau_\mathrm{frag}/T_\mathrm{orb}$	$\tau_\mathrm{coag}/T_\mathrm{orb}$
Average midplane	0.5	30	90
Peak midplane	100.0	0.15	0.45
Contracting cluster	1000.0	0.015	0.045

Table 8: Estimated time-scales, in units of orbits, for collisional fragmentation and for coagulation in three different states of the mid-plane layer.

pressure support on the maximum density of solids. We show in Fig. 27 the topography of the sedimented particle layer and the maximum particle density of two 64^3 simulations: the standard run with $(\partial \ln P/\partial \ln r)H/r = -0.04$ and a run with higher radial pressure support and $(\partial \ln P/\partial \ln r)H/r = -0.1$. The same comparison at 128^3 is shown in the main text. The increased radial pressure support, $\Delta v = -0.05 c_\mathrm{s}$, is very clear in the latter case from the tilted particle bands, but the streaming instability still produces radial overdensities. We have checked the column density required for gravitational collapse in models with $\Delta v = -0.05 c_\mathrm{s}$ and found that approximately a factor two higher value of the column density of gas is needed for the collapse (see Table 7) compared to the standard model with $\Delta v = -0.02 c_\mathrm{s}$.

1.15 Other processes

In order to isolate the effect of self-gravity on the dynamics of the solids we have ignored two potentially important collisional effects: coagulation and collisional fragmentation. In this section we estimate time-scales and effects of these physical phenomena.

The time-scale of collisions is

$$\tau_\mathrm{coll} = \frac{\tau_\mathrm{f}}{(c_\mathrm{p}/c_\mathrm{s})(\rho_\mathrm{p}/\rho_\mathrm{g})}\,, \tag{48}$$

where c_p is the collision speed of the boulders and τ_f is the friction time. Assuming spherical boulders gives the relation

$$\frac{a_\bullet}{\dot{a}_\bullet} = 3\frac{m_\bullet}{\dot{m}_\bullet} \tag{49}$$

between the time-scale for radius doubling and the time-scale for mass doubling, which in turn is just the collisional time-scale. We consider regions with solid-to-gas ratios characteristic of the average midplane in a turbulent disc, the peak density in the turbulent midplane, and an intermediate density in a gravitationally contracting cluster, as described in Table 8. The same table gives the time-scales for collisional fragmentation and for coagulation for these different regions.

The average state has a coagulation time of close to 100 orbits, comparable to the time-scale for radial drift in. To cross the drift barrier effectively a few coagulation times are needed, so the growing solids are lost into the inner disc before they can decouple from the gas. A more advanced model would take into account the sweep up of small grains as the boulders drift, but essentially the same result is reached[79].

The size of the boulders could increase on the time-scale of only one orbit in the overdense particle clusters that occur in transient high pressure regions and due to the streaming insta-

bility. Coagulation could go even faster in the gravitationally contracting regions. This may be how planetesimals eventually form: by coagulation in an overdense environment set by the self-gravity of the solids. The strength of the scenario presented in the main text, though, is that it does not rely on coagulation being efficient in same way as pure coagulation models do[28,27]. Coagulation is needed to build up marginally coupled solids—metre-sized boulders at 5 AU or centimetre-sized pebbles at 40 AU—but does not directly drive gravitational collapse.

Collisional fragmentation may also be prevalent in gravitationally contracting clusters. In that case one can speculate that the mode of radius growth is by sweeping up of collisional fragments by the few lucky boulders that avoid catastrophic collisions with equal-sized bodies.

Supplementary Notes

1. Safronov, V. S. *Evoliutsiia Doplanetnogo Oblaka.* (English transl.: Evolution of the protoplanetary cloud and formation of Earth and the planets, NASA Tech. Transl. F-677, Jerusalem: Israel Sci. Transl. 1972, 1969).

2. Dominik, C., Blum, J., Cuzzi, J. N. & Wurm, G. Growth of dust as the initial step toward planet formation. In Reipurth, B., Jewitt, D. & Keil, K. (eds.) *Protostars and Planets V*, 783–800 (2007).

3. Benz, W. Low velocity collisions and the growth of planetesimals. *Space Science Reviews* **92**, 279–294 (2000).

4. Weidenschilling, S. J. Aerodynamics of solid bodies in the solar nebula. *Mon. Not. R. Astron. Soc.* **180**, 57–70 (1977).

5. Goldreich, P. & Ward, W. R. The formation of planetesimals. *Astrophys. J.* **183**, 1051–1062 (1973).

6. Youdin, A. N. & Shu, F. H. Planetesimal formation by gravitational instability. *Astrophys. J.* **580**, 494–505 (2002).

7. Weidenschilling, S. J. & Cuzzi, J. N. Formation of planetesimals in the solar nebula. In Levy, E. H. & Lunine, J. I. (eds.) *Protostars and Planets III*, 1031–1060 (1993).

8. Hartmann, L. *Accretion processes in star formation* (Accretion processes in star formation / Lee Hartmann. Cambridge, UK ; New York : Cambridge University Press, 1998. (Cambridge astrophysics series ; 32) ISBN 0521435072., 1998).

9. Johansen, A., Klahr, H. & Henning, T. Gravoturbulent formation of planetesimals. *Astrophys. J.* **636**, 1121–1134 (2006).

10. Youdin, A. N. & Goodman, J. Streaming instabilities in protoplanetary disks. *Astrophys. J.* **620**, 459–469 (2005).

11. Johansen, A., Henning, T. & Klahr, H. Dust sedimentation and self-sustained Kelvin-Helmholtz turbulence in protoplanetary disk midplanes. *Astrophys. J.* **643**, 1219–1232 (2006).

12. Johansen, A. & Youdin, A. Protoplanetary Disk Turbulence Driven by the Streaming Instability: Nonlinear Saturation and Particle Concentration. *Astrophys. J.* **662**, 627–641 (2007).

13. Cuzzi, J. N., Dobrovolskis, A. R. & Champney, J. M. Particle-gas dynamics in the midplane of a protoplanetary nebula. *Icarus* **106**, 102–134 (1993).

14. Balbus, S. A. & Hawley, J. F. Instability, turbulence, and enhanced transport in accretion disks. *Reviews of Modern Physics* **70**, 1–53 (1998).

15. Barge, P. & Sommeria, J. Did planet formation begin inside persistent gaseous vortices? *Astron. Astrophys.* **295**, L1–L4 (1995).

16. Fromang, S. & Nelson, R. P. On the accumulation of solid bodies in global turbulent protoplanetary disc models. *Mon. Not. R. Astron. Soc.* **364**, L81–L85 (2005).

17. Rice, W. K. M., Lodato, G., Pringle, J. E., Armitage, P. J. & Bonnell, I. A. Planetesimal formation via fragmentation in self-gravitating protoplanetary discs. *Mon. Not. R. Astron. Soc.* **372**, L9–L13 (2006).

18. Cuzzi, J. N., Hogan, R. C., Paque, J. M. & Dobrovolskis, A. R. Size-selective concentration of chondrules and other small particles in protoplanetary nebula turbulence. *Astrophys. J.* **546**, 496–508 (2001).

19. Hockney, R. W. & Eastwood, J. W. *Computer simulation using particles* (New York: McGraw-Hill, 1981).

20. Gammie, C. F. Nonlinear outcome of gravitational instability in cooling, gaseous disks. *Astrophys. J.* **553**, 174–183 (2001).

21. Gammie, C. F. Layered accretion in T Tauri disks. *Astrophys. J.* **457**, 355–362 (1996).

22. Tanga, P., Weidenschilling, S. J., Michel, P. & Richardson, D. C. Gravitational instability and clustering in a disk of planetesimals. *Astron. Astrophys.* **427**, 1105–1115 (2004).

23. Salo, H. Gravitational wakes in Saturn's rings. *Nature* **359**, 619–621 (1992).

24. Boss, A. P. Giant planet formation by gravitational instability. *Science* **276**, 1836–1839 (1997).

25. Mayer, L., Quinn, T., Wadsley, J. & Stadel, J. Formation of giant planets by fragmentation of protoplanetary disks. *Science* **298**, 1756–1759 (2002).

26. Weidenschilling, S. J. Can gravitational instability form planetesimals? *Icarus* **116**, 433–435 (1995).

27. Dullemond, C. P. & Dominik, C. Dust coagulation in protoplanetary disks: A rapid depletion of small grains. *Astron. Astrophys.* **434**, 971–986 (2005).

28. Weidenschilling, S. J. The origin of comets in the solar nebula: A unified model. *Icarus* **127**, 290–306 (1997).

29. Throop, H. B. & Bally, J. Can Photoevaporation Trigger Planetesimal Formation? *Astrophys. J.* **623**, L149–L152 (2005).

30. Haghighipour, N. & Boss, A. P. On pressure gradients and rapid migration of solids in a nonuniform solar nebula. *Astrophys. J.* **583**, 996–1003 (2003).

31. Brandenburg, A. *Computational aspects of astrophysical MHD and turbulence*, 269–+ (Advances in Nonlinear Dynamos, 2003). `http://www.arxiv.org/astro-ph/0109497/`.

32. Haugen, N. E. & Brandenburg, A. Inertial range scaling in numerical turbulence with hyperviscosity. *Phys. Rev. E* **70**, 026405–+ (2004).

33. Johansen, A. & Klahr, H. Dust diffusion in protoplanetary disks by magnetorotational turbulence. *Astrophys. J.* **634**, 1353–1371 (2005).

34. Brandenburg, A. & Sarson, G. R. Effect of hyperdiffusivity on turbulent dynamos with helicity. *Physical Review Letters* **88**, 055003–+ (2002).

35. Biskamp, D. & Müller, W.-C. Scaling properties of three-dimensional isotropic magnetohydrodynamic turbulence. *Physics of Plasmas* **7**, 4889–4900 (2000).

36. Sano, T., Inutsuka, S.-i., Turner, N. J. & Stone, J. M. Angular momentum transport by magnetohydrodynamic turbulence in accretion disks: Gas pressure dependence of the saturation level of the magnetorotational instability. *Astrophys. J.* **605**, 321–339 (2004).

37. Youdin, A. & Johansen, A. Protoplanetary Disk Turbulence Driven by the Streaming Instability: Linear Evolution and Numerical Methods. *Astrophys. J.* **662**, 613–626 (2007).

38. Hayashi, C. Structure of the solar nebula, growth and decay of magnetic fields and effects of magnetic and turbulent viscosities on the nebula. *Prog. Theor. Phys.* **70**, 35–53 (1981).

39. Nakagawa, Y., Sekiya, M. & Hayashi, C. Settling and growth of dust particles in a laminar phase of a low-mass solar nebula. *Icarus* **67**, 375–390 (1986).

40. Chapman, S. & Cowling, T. G. *The mathematical theory of non-uniform gases. an account of the kinetic theory of viscosity, thermal conduction and diffusion in gases* (Cambridge: University Press, 1970, 3rd ed., 1970).

41. Dobrovolskis, A. R., Dacles-Mariani, J. S. & Cuzzi, J. N. Production and damping of turbulence by particles in the solar nebula. J. Geophys. Res. **104**, 30805–+ (1999).

42. Youdin, A. N. Planetesimal formation without thresholds. I: Dissipative gravitational instabilities and particle stirring by turbulence. *ArXiv Astrophysics e-prints* (2005). `http://arxiv.org/abs/astro-ph/astro-ph/0508659/`.

43. Toomre, A. On the gravitational stability of a disk of stars. *Astrophys. J.* **139**, 1217–1238 (1964).

44. Spitzer, L. J. The dynamics of the interstellar medium. III. Galactic distribution. *Astrophys. J.* **95**, 329–+ (1942).

45. Epstein, P. S. On the resistance experienced by spheres in their motion through gases. *Physical Review* **23**, 710–733 (1924).

46. Garzó, V. & Dufty, J. W. Dense fluid transport for inelastic hard spheres. *Phys. Rev. E* **59**, 5895–5911 (1999).

47. Hartmann, W. K. Impact experiments. I - Ejecta velocity distributions and related results from regolith targets. *Icarus* **63**, 69–98 (1985).

48. Hawley, J. F., Gammie, C. F. & Balbus, S. A. Local three-dimensional magnetohydrodynamic simulations of accretion disks. *Astrophys. J.* **440**, 742 (1995).

49. Stepinski, T. F. & Valageas, P. Global evolution of solid matter in turbulent protoplanetary disks. I. Aerodynamics of solid particles. *Astron. Astrophys.* **309**, 301–312 (1996).

50. Youdin, A. N. & Chiang, E. I. Particle pileups and planetesimal formation. *Astrophys. J.* **601**, 1109–1119 (2004).

51. Bate, M. R. & Burkert, A. Resolution requirements for smoothed particle hydrodynamics calculations with self-gravity. *Mon. Not. R. Astron. Soc.* **288** (1997).

52. Truelove, J. K. *et al.* Self-gravitational hydrodynamics with three-dimensional adaptive mesh refinement: Methodology and applications to molecular cloud collapse and fragmentation. *Astrophys. J.* **495**, 821–852 (1998).

53. Wisdom, J. & Tremaine, S. Local simulations of planetary rings. *Astron. J.* **95**, 925–940 (1988).

54. Truelove, J. K. *et al.* The jeans condition: A new constraint on spatial resolution in simulations of isothermal self-gravitational hydrodynamics. *Astrophys. J.* **489**, L179+ (1997).

55. Li, Y., Mac Low, M.-M. & Klessen, R. S. Star formation in isolated disk galaxies. I. Models and characteristics of nonlinear gravitational collapse. *Astrophys. J.* **626**, 823–843 (2005).

56. Nelson, A. F. Numerical requirements for simulations of self-gravitating and non-self-gravitating discs. *Mon. Not. R. Astron. Soc.* **373**, 1039–1073 (2006).

57. Bate, M. R., Bonnell, I. A. & Price, N. M. Modelling accretion in protobinary systems. *Mon. Not. R. Astron. Soc.* **277** (1995).

58. Youdin, A. N. Planetesimal formation without thresholds. II: Gravitational instability of solids in turbulent protoplanetary disks. *ArXiv Astrophysics e-prints* (2005). `http://arxiv.org/abs/astro-ph/astro-ph/0508662/`.

59. Ward, W. R. The formation of the solar system. In *Frontiers of Astrophysics,* ed. E.H. Avrett, 1–40 (1976).

60. Ward, W. R. *On planetesimal formation: The role of collective particle behavior*, 75–84 (Origin of the earth and moon, edited by R.M. Canup and K. Righter and 69 collaborating authors. Tucson: University of Arizona Press., p.75-84, 2000).

61. Ryan, E. V., Davis, D. R. & Giblin, I. A laboratory impact study of simulated Edgeworth-Kuiper belt objects. *Icarus* **142**, 56–62 (1999).

62. Youdin, A. N. & Lithwick, Y. Particle Stirring in Turbulent Gas Disks: Including Orbital Oscillations. *Submitted to Icarus* (2007).

63. Johansen, A., Klahr, H. & Mee, A. J. Turbulent diffusion in protoplanetary discs: the effect of an imposed magnetic field. *Mon. Not. R. Astron. Soc.* **370**, L71–L75 (2006). `astro-ph/0603765`.

64. Shakura, N. I., Sunyaev, R. A. & Zilitinkevich, S. S. On the turbulent energy transport in accretion discs. *Astron. Astrophys.* **62**, 179–187 (1978).

65. Dubrulle, B., Morfill, G. & Sterzik, M. The dust subdisk in the protoplanetary nebula. *Icarus* **114**, 237–246 (1995).

66. Voelk, H. J., Morfill, G. E., Roeser, S. & Jones, F. C. Collisions between grains in a turbulent gas. *Astron. Astrophys.* **85**, 316–325 (1980).

67. Blaes, O. M. & Balbus, S. A. Local shear instabilities in weakly ionized, weakly magnetized disks. *ApJ* **421**, 163 (1994).

68. Fromang, S., Terquem, C. & Balbus, S. A. The ionization fraction in α models of protoplanetary discs. *Mon. Not. R. Astron. Soc.* **329**, 18–28 (2002).

69. Semenov, D., Wiebe, D. & Henning, T. Reduction of chemical networks. II. Analysis of the fractional ionisation in protoplanetary discs. *Astron. Astrophys.* **417**, 93–106 (2004).

70. Ilgner, M. & Nelson, R. P. On the ionisation fraction in protoplanetary disks. II. The effect of turbulent mixing on gas-phase chemistry. *Astron. Astrophys.* **445**, 223–232 (2006).

71. Sano, T., Miyama, S. M., Umebayashi, T. & Nakano, T. Magnetorotational instability in protoplanetary disks. II. Ionization state and unstable regions. *Astrophys. J.* **543**, 486–501 (2000).

72. Inutsuka, S.-i. & Sano, T. Self-sustained Ionization and Vanishing Dead Zones in Protoplanetary Disks. *Astrophys. J.* **628**, L155–L158 (2005). `arXiv:astro-ph/0506131`.

73. Ilgner, M. & Nelson, R. P. On the ionisation fraction in protoplanetary disks. III. The effect of X-ray flares on gas-phase chemistry. *Astron. Astrophys.* **455**, 731–740 (2006). `arXiv:astro-ph/0605290`.

74. Fleming, T. & Stone, J. M. Local magnetohydrodynamic models of layered accretion disks. *Astrophys. J.* **585**, 908–920 (2003).

75. Turner, N. J., Sano, T. & Dziourkevitch, N. Turbulent Mixing and the Dead Zone in Protostellar Disks. *Astrophys. J.* **659**, 729–737 (2007). `arXiv:astro-ph/0612552`.

76. Oishi, J. S., Mac Low, M.-M. & Menou, K. Turbulent Torques on Protoplanets in Dead Zones. *submitted to Astrophys. J.* (2007). `arXiv:astro-ph/0702549`.

77. Weidenschilling, S. J. Dust to planetesimals - settling and coagulation in the solar nebula. *Icarus* **44**, 172–189 (1980).

78. Gómez, G. C. & Ostriker, E. C. The effect of the Coriolis force on Kelvin-Helmholtz-driven mixing in protoplanetary disks. *Astrophys. J.* **630**, 1093–1106 (2005).

79. Klahr, H. & Bodenheimer, P. Formation of giant planets by concurrent accretion of solids and gas inside an anticyclonic vortex. *Astrophys. J.* **639**, 432–440 (2006).